remote sensing

MDPI

Article

Harnessing Multi-Source Data and Deep Learning for High-Resolution Land Surface Temperature Gap-Filling Supporting Climate Change Adaptation Activities

Katja Kustura, David Conti, Matthias Sammer and Michael Riffler *

GeoVille Information Systems and Data Processing GmbH, A-6020 Innsbruck, Austria; kustura@geoville.com (K.K.); conti@geoville.com (D.C.); sammer@geoville.com (M.S.)
* Correspondence: riffler@geoville.com

Abstract: Addressing global warming and adapting to the impacts of climate change is a primary focus of climate change adaptation strategies at both European and national levels. Land surface temperature (LST) is a widely used proxy for investigating climate-change-induced phenomena, providing insights into the surface radiative properties of different land cover types and the impact of urbanization on local climate characteristics. Accurate and continuous estimation across large spatial regions is crucial for the implementation of LST as an essential parameter in climate change mitigation strategies. Here, we propose a deep-learning-based methodology for LST estimation using multi-source data including Sentinel-2 imagery, land cover, and meteorological data. Our approach addresses common challenges in satellite-derived LST data, such as gaps caused by cloud cover, image border limitations, grid-pattern sensor artifacts, and temporal discontinuities due to infrequent sensor overpasses. We develop a regression-based convolutional neural network model, trained on ECOSTRESS (ECOsystem Spaceborne Thermal Radiometer Experiment on Space Station) mission data, which performs pixelwise LST predictions using 5×5 image patches, capturing contextual information around each pixel. This method not only preserves ECOSTRESS's native resolution but also fills data gaps and enhances spatial and temporal coverage. In non-gap areas validated against ground truth ECOSTRESS data, the model achieves LST predictions with at least 80% of all pixel errors falling within a ± 3 °C range. Unlike traditional satellite-based techniques, our model leverages high-temporal-resolution meteorological data to capture diurnal variations, allowing for more robust LST predictions across different regions and time periods. The model's performance demonstrates the potential for integrating LST into urban planning, climate resilience strategies, and near-real-time heat stress monitoring, providing a valuable resource to assess and visualize the impact of urban development and land use and land cover changes.

Keywords: climate change adaptation; urban heat island; land surface temperature; ECOSTRESS; Sentinel-2; INCA; deep learning; convolutional neural network; gap-filling

Academic Editor: Ashraf Dewan

Received: 11 November 2024
Revised: 13 January 2025
Accepted: 13 January 2025
Published: 17 January 2025

Citation: Kustura, K.; Conti, D.; Sammer, M.; Riffler, M. Harnessing Multi-Source Data and Deep Learning for High-Resolution Land Surface Temperature Gap-Filling Supporting Climate Change Adaptation Activities. *Remote Sens.* **2025**, *17*, 318. https://doi.org/10.3390/rs17020318

1. Introduction

Responding to global warming and adapting to climate change effects such as heat waves and drought is a key priority for stakeholders involved in the definition of climate change adaptation strategies [1]. Most of the largest cities experience profound changes due to urbanization and hence, city administrations are facing challenges in safeguarding high-quality urban growth despite increasingly tight spatial resources. Studies have shown that the degree of surface sealing has a direct impact on the radiation balance by modifying

the surface radiative properties and radiatively active air pollutants [2,3], thus influencing the ratio between sensible and latent heat fluxes. These modifications in a built-up environment make cities (but also smaller municipalities) warmer than their surroundings and more prone to excess heat, leading to an urban heat island (UHI) effect [4]. Other studies have demonstrated that the temperature within urbanized areas shows a high degree of variability depending on the local urban morphology [5–7]. Land use and land cover, along with their changes in general, influence the local climate characteristics [8,9]. Regional and city administrations make use of this knowledge, aiming to reduce health risks related to climate change and to increase human well-being by implementing heat mitigation measures such as green and blue infrastructure [10,11]. Altering thermal comfort in urban environments enhances the time of exposure to an uncomfortable amount of heat. This can be particularly dangerous for vulnerable individuals, as well as for those performing strenuous physical work in high heat, potentially leading to fatal outcomes [12–14]. Moreover, recent studies have highlighted that climate change in general, and increasing temperatures in particular, pose a significant risk for mountainous areas, affecting alpine communities and their economy (e.g., tourism) [15]. Global and regional warming can further amplify the effect of excess heat [16]. Taking adaptive measures is not only the focus of larger cities but also of any urban area and mountainous region. Understanding how land use and climate trends impact local climates is essential for decision-makers to develop cost-effective, evidence-based, and consistent solutions for sustainable cities and for rural and mountainous communities. The goal of our study is, therefore, the development of a methodology allowing the local heat variability to be highlighted at high resolution (compared to numerical weather prediction model output) and based on actual observations from satellite sensors, with the overall aim to support climate change adaptation activities at a local and regional scale.

Land Surface Temperature (LST) is a proxy that is broadly used to investigate the Surface Urban Heat Island (SUHI) effect [4,17]. The positive correlation between LST and the degree of surface sealing [18,19] represents the intensity of the SUHI which, identical to the UHI effect, is higher in urban environments compared to rural areas [18]. The degree of surface sealing is also related to the Bowen ratio (β; ratio between sensible and latent heat fluxes) [20]. Surfaces with a higher Bowen ratio ($\beta > 1$) indicate lower soil moisture availability [21], leading to an increase in LST, enhanced heat exchange by convection, and an increase in near-surface air temperatures [22], thus intensifying urban heat [18,19]. Conversely, surfaces with a lower Bowen ratio ($\beta < 1$) indicate higher soil moisture availability [21], which decreases LST and favors the evapotranspiration-driven cooling effect, leading to a decrease in near-surface air temperatures [23]. LST is a crucial parameter in numerous fields, including surface energy and water balance, ecology, agriculture, environment, climatology, meteorology, and hydrology [24–26], contributing to an overall understanding of the Earth's surface dynamics and the impact of climate trends. Improving our understanding of LST and its interplay with surface sealing, land cover, and meteorological conditions is thus paramount, with a wide range of applications involving Surface Heat Island, urban climate studies [27–29], drought monitoring [30], surface soil moisture and evapotranspiration estimation [31,32], and numerical weather prediction, to name a few.

A major advantage of using LST to investigate the SUHI effect is its availability from gridded data (e.g., Earth-observation (EO)-based retrieval), which enables the analysis of local effects depending on the resolution of the satellite sensor. In addition, a remote-sensing-based LST dataset has been accepted by the International Geosphere and Biosphere Program as one of the high-priority parameters, and the Global Climate Observing System identified it as an Essential Climate Variable [33]. EO-based LST represents the accumula-

tive radiometric surface temperature of all materials of the surface cover within the sensor's field of view [34]. Thus, LST estimation from thermal infrared images is complex due to the surface composition, with materials of varying emissivity and geometry [35–38]. For example, a densely vegetated area represents the surface temperature of vegetation; whereas in a sparsely vegetated area, the surface temperature includes contributions from vegetation and soil simultaneously [36]. EO-based retrieval of LST has a long tradition dating back to the 1960s with the launch of the TIROS-II satellite [39,40]. Numerous EO sensors subsequently followed, carried on geostationary and low-Earth-orbit satellites and providing data at coarse spatial resolutions (750 m to 4 km, e.g., Geostationary Operational Environmental Satellite, GOES [41]; Spinning Enhanced Visible and Infrared Imager, SEVIRI [42]; Advanced Very High Resolution Radiometer, AVHRR [43]; Moderate-resolution Imaging Spectroradiometer, MODIS [44]; Advanced Along-Track Scanning Radiometer, AATSR [45]; Visible Infrared Imaging Radiometer Suit, VIIRS [46]; Sentinel-3 Sea and Land Surface Temperature Radiometer, SLSTR [47]). Medium spatial resolution data (70 to 100 m) is provided through sensors such as the Advanced Spaceborne Thermal Emission and Reflection Radiometer (ASTER, e.g., [48]), the Landsat Thermal Infrared Sensor (TIRS) [49], and the ECOsystem Spaceborne Thermal Radiometer Experiment on Space Station (ECOSTRESS) [50]. In the context of EO-based LST retrieval, the impact of spatial resolution is significant, as higher-resolution sensors provide more precise insights into localized heat variations [51], which can be particularly important for capturing the UHI effect in urban areas with heterogeneous surfaces.

Satellite-based LST datasets have been extensively used, e.g., for advanced assessments of UHI effects—overcoming the challenges of conducting high-resolution air temperatures at similar scale [27]—in assessment and mitigation studies elaborating on the spatiotemporal behavior of the UHIs [52–58] and in downscaling studies, providing high-resolution LST maps based on the assumption of a scale-invariant relationship between LST and other influencing parameters (e.g., surface sealing degree, reflectance, spectral indices) [57,59–62]. These advances establish LST as an essential parameter for advanced applications in urban and built-up environments. A particularly interesting approach consists of integrating methods operating at different scales to enhance modeling capabilities in heat assessment studies; namely, the integration of LST datasets with the Computational Fluid Dynamics–Geographic Information System integrated modeling approach [6,7]—enabling modeling of the SUHI effect at very high spatial resolution—and urban climate models used to downscale and evaluate the localized effects of heat or other climate-related parameters [63]. A critical requirement for fully utilizing LST within a multi-resolution and multi-sensor data fusion methodology is access to a comprehensive LST dataset provided on a high spatial and temporal distribution. Satellite missions like ECOSTRESS and Landsat offer high-resolution LST data at sub-100 m scales; however, their usability is limited by sparse temporal coverage due to infrequent overpass schedules and cloud interference. These limitations create significant data gaps, particularly in regions with persistent cloud cover, thus reducing the availability and continuity of LST observations, and necessitating the development of gap-filling techniques.

Interest in LST gap-filling methodologies grew in the 2010s, driven by the challenges coming from incomplete satellite data caused by cloud cover, sensor limitations, and infrequent overpass times [64–67]. The methodologies for LST gap-filling have evolved rapidly, resulting in various techniques that can be categorized into several distinct approaches [65,66]. Reconstruction methods—which can be either spatial, temporal, or spatiotemporal—exploit spatial and temporal correlations, using neighboring pixels in space and time to estimate missing values (e.g., [68–72]). These methods are effective at filling gaps in existing data, but they result in hypothetical, clear-sky LST estimates.

Data fusion methods combine multiple data sources, such as satellite-derived and passive microwave data, to improve the accuracy of LST predictions by integrating information from different datasets (e.g., [73]). This approach enables LST estimates even in areas with cloud cover. Surface energy balance methods are employed to estimate LST under clouds by considering physical parameters like radiation and atmospheric conditions (e.g., [74,75]). Temporal gap-filling techniques address the issue of missing data due to sparse satellite overpasses, using methods such as temporal interpolation and diurnal temperature cycle modeling to reconstruct missing values from the time series data (e.g., [76,77]). Spatiotemporal data fusion combines data from multiple sensors, such as MODIS and Landsat, to enhance both spatial and temporal resolution [78]. Additionally, simulated data can be incorporated within fusion frameworks, allowing for more precise and continuous LST predictions across time and space [77].

Over the past decade, machine learning models have become integral to the field of Earth observation, with numerous pivotal reviews highlighting the breakthroughs in remote sensing, and applications in image processing, data fusion, time series analysis, object detection, and land cover mapping [79–84]. In recent years, machine learning techniques have been increasingly adopted for LST gap-filling, leveraging their capacity to model complex relationships between LST and auxiliary data sources ([67] and references therein). Methods such as multiple linear regression, random forest, and deep learning have been applied successfully to map all-weather LST [68,85–88]. The combination of traditional physical models with machine learning algorithms has further improved the accuracy and spatial–temporal resolution of LST products [89]. Convolutional neural networks (CNNs), in particular, have been investigated due to their ability to learn relationships between neighboring pixels in an image, enabling the extraction and learning of complex spatial features [79,80]. While they have been popular for classification and segmentation tasks [90–92], regression-based CNN models are becoming increasingly prevalent, facilitating the estimation of continuous data in environmental, urban, and agricultural contexts [82]. These models have shown promising applications for both surface and air temperature predictions [84,88,93,94], highlighting their potential in advancing LST gap-filling methodologies.

The objective of this study is to develop a deep-learning-based methodology for estimating LST using multi-source data, and to demonstrate its potential applicability in the context of urban climate resilience strategies and near-real-time heat stress monitoring. The main contributions can be summarized as follows. (1) A lightweight, regression-based CNN model is developed to predict LST from multi-source data, including Sentinel-2 data, land cover information, and hourly meteorological data. The network is trained on ECOSTRESS data, and it can learn highly dynamic spatiotemporal relationships between ECOSTRESS and the auxiliary datasets, enabling LST estimation based solely on the current meteorological conditions and land characteristics. In other words, LST is not required as an input. (2) Since the network does not require LST as the input, it can generate predictions at any location on an hourly basis, given the availability of meteorological data. This approach provides both spatial and temporal gap-filling of the ECOSTRESS images, addressing simultaneously the gaps due to cloud cover and sensor limitations, as well as the temporal discontinuities in the data availability. The model can thereby generate high-quality LST data across large spatial regions and with high temporal resolution. (3) The model is validated over urban areas, demonstrating the potential to integrate and use the developed methodology in urban climate modeling approaches and spatial planning activities [6,7,47].

The paper is organized as follows. In Section 2, we describe the materials, including the areas of interest and the datasets, and provide details on the processing methodology. In

Section 3, we present the model results and analyze LST predictions in spatial and temporal contexts. The discussion and conclusions are provided in Sections 4 and 5, respectively.

2. Materials and Methodology

2.1. Study Areas

We selected two areas of interest for our study (AREA I and II), covering various land cover classes within the urban, rural, and alpine environment.

AREA I, located at approximately 47.27°N and 11.39°E and covering 19.3 × 16.3 km^2, includes the city of Innsbruck, Austria, and its surrounding area (see Figure 1). The city region includes the typical heterogeneous urban environments (such as buildings and roads), vegetated areas (parks, lawns), and bodies of water (rivers, lakes). The area outside of the city borders includes rural and agricultural features, as well as typical alpine features such as mountainous terrain, forests, and meadows. Innsbruck has a humid continental climate with highly variable summers, and a June–July daily mean temperature of 18.9 °C [95,96].

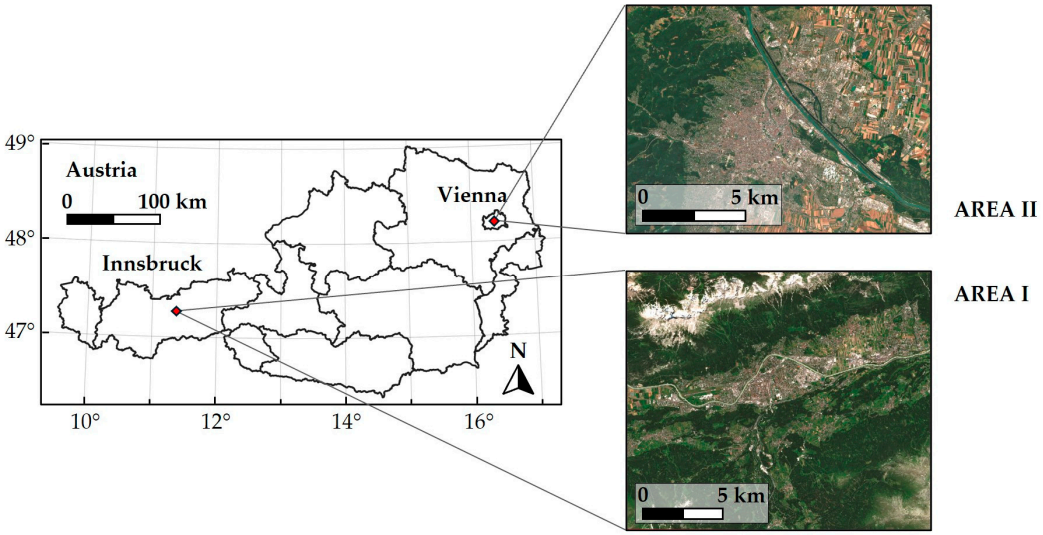

Figure 1. Location of the two areas of interest within Austria: AREA I (Innsbruck; WGS84 coordinates 47.27°N, 11.39°E), AREA II (Vienna; WGS84 coordinates 48.21°N, 16.37°E). The zoomed-in insets are displayed with standard true color composites.

AREA II, located at approximately 48.21°N and 16.37°E and covering 29.8 × 22.4 km^2, includes the city of Vienna, Austria, and its surrounding area (see Figure 1). The city region is characterized by typical urban areas, such as residential, commercial and industrial areas, as well as vegetated and water areas. The greater region also includes extensive agricultural surfaces and forests. Vienna has a borderline oceanic and humid continental climate with warm summers, and a June–July daily mean temperature of 21.2 °C [95,96].

The primary application of interest within our study being heat monitoring, we focus on the analysis of LST trends during summer months. Therefore, we define our time window of interest as the summer months of June, July, and August. For the preparation of the datasets described in the following subsections, we focus on the data available from the years 2022 and 2023. The data obtained within such constraints are thus a representation of typical summer conditions in AREA I and AREA II.

2.2. Land Surface Temperature

The primary objective of this study is the development of a neural-network-based model capable of capturing and predicting dense LST time series over large spatial regions. Achieving this goal strongly relies on the careful selection of input datasets, a crucial step

that underpins the modeling process. In the input data selection, we have been guided by the established theoretical models for LST, which provide the essential framework for relating the LST to the various physical parameters characterizing the surface and the surrounding environment.

LST is a key environmental metric that measures the radiative skin temperature of the Earth's surface. Unlike air temperature, which is typically measured at weather stations and reflects the atmospheric conditions above ground, LST encompasses thermal infrared radiation emitted by the land surface. Consequently, it is strongly dependent on atmospheric dynamics, global radiation, and the reflective and absorptive surface characteristics [6,97–99]. The dependence on these various parameters is captured by a physical model, which provides an empirical formula relating LST to atmospheric and surface conditions [97,98]:

$$T_{\text{surface}} = T_{\text{air}} + \frac{Q + B}{(6.2 + 4.26 \times v_{\text{wind}})\left(1 + \frac{1}{\beta}\right)} \tag{1}$$

Here, T_{surface} and T_{air} denote the surface and air temperature, respectively, Q represents the net all-wave radiation flux, B represents the substrate heat flux, v_{wind} is wind speed, and β is the Bowen ratio [20]. The model in Equation (1) captures the fundamental relationships governing LST in relation to ambient and surface parameters. However, it is of limited practical use, its utility being constrained by the demand for precise calculations of multiple heat fluxes, a task that is often challenging and spatially limited. Instead, we opt for a more robust approach, leveraging a neural-network-based methodology, as described in more detail in Section 2.4, and we base our selection of input parameters on the physical model given by Equation (1).

In particular, the parameters T_{air}, Q, B, v_{wind} represent variables dependent on ambient meteorological conditions, while the Bowen ratio β elucidates the relationship between sensible heat and latent heat, depending on factors such as surface type (e.g., vegetation, water, urban), weather conditions, and time of day [100]. With our choice of input parameters, we carefully address and encompass the elements from the physical model into our neural network model, ensuring a model that is both physically meaningful and computationally robust.

2.3. Datasets

The modeling workflow presented in this study makes use of multiple datasets, which are summarized in Table 1 and described in more detail in the following subsections. The thermal data consists of the ECOSTRESS 70 m LST product (Section 2.3.1) which also defines the target resolution in our gap-filling procedure. The meteorological data is provided by the Integrated Nowcasting through Comprehensive Analysis (INCA) dataset of the Austrian national meteorological service (Section 2.3.2) and the optical multispectral data includes Sentinel-2 imagery (Section 2.3.3). Additional land cover and topographic datasets are described in Section 2.3.4. Due to the different spatial resolutions of the input datasets, various resampling techniques have been applied to the datasets in preparation for the gap-filling process (cf. Table 1). To address temporal differences in the datasets, we selected the closest available timestamps per dataset, which in the case of the meteorological data is within one hour, for Sentinel-2 is the closest cloud-free observation, and for the land cover is the last published dataset (currently 2018). We assume that the variability of the underlying land surface characteristics (i.e., albedo from Sentinel-2 multi-spectral data and land cover changes) are negligible and have a minor effect on the overall error.

Table 1. Summary of the datasets used in this study. The column 'Resampling Method' indicates the spatial (S) and temporal (T) resampling applied to the datasets.

Dataset (Source)	Resolution	Resampling Method	Considered Parameters
ECOSTRESS-LSTE (ECOSTRESS)	70 m	Target resolution	Land surface temperature, quality control
INCA (Geosphere Austria)	1 km	S: Bilinear interpolation T: Nearest observation (<1 h)	Air temperature at 2 m, relative humidity at 2 m, global radiation, wind speed
Sentinel-2 (Sentinel-2 mission)	10/20 m	S: Mean aggregation T: Nearest observation (<1 month)	Bands B2, B3, B4, B8, B11, B12
EU-DEM (Copernicus Land Monitoring Service)	25 m	S: Nearest neighbor T: NA	Elevation, aspect, slope
Land cover (Copernicus Land Monitoring Service)	10 m	S: Nearest neighbor T: 2018	Tree cover density, water and wetness index, imperviousness

2.3.1. ECOSTRESS: Target Dataset

ECOSTRESS is an ongoing NASA scientific mission mounted on the International Space Station (ISS). The main instrument in ECOSTRESS is a multispectral thermal infrared radiometer, which collects and provides measurements of the surface temperature [101]. We use the ECOSTRESS Land Surface Temperature and Emissivity (ECOSTRESS-LSTE) Level 2 dataset for the supervised learning approach. The ECOSTRESS-LSTE L2 product is provided in 70 m resolution, with irregular revisit times of one to five days according to the flight pattern of the ISS [102]. Due to the inclined and precessing orbit of the ISS, the observation times of the ECOSTRESS instrument vary, with some days providing multiple observations per day [50]. Spatially, ECOSTRESS observations usually cover a large geographic area; specifically, a single ECOSTRESS-LSTE observation is typically sufficient to reproduce a single scene over our areas of interest.

The corresponding ECOSTRESS data acquisition follows via an automated download directly from the NASA search portal [103]. ECOSTRESS-LSTE is the cornerstone dataset of our model, providing target values for the supervised learning of LST. An example ECOSTRESS LST observation is shown in Figure 2a.

2.3.2. INCA

The INCA dataset is a temporally detailed meteorological dataset provided by the Central Institute for Meteorology and Geodynamics in Austria. The INCA data is modeled using various available data sources—station observations, remote sensing data, numerical weather prediction models and a high-resolution terrain model—to produce the analysis of the current state of the near-ground atmosphere [104]. INCA data is provided at a 1 km spatial and an hourly temporal resolution, with historical data available dating back to 2013. The dataset covers five weather-relevant parameters which we consider as the input: air temperature, global radiation, relative humidity, and wind speed in two directions. An example INCA air temperature observation is shown in Figure 2b. This comprehensive coverage offers a view of weather conditions at any given location, and it provides many of the essential physical parameters required by the physical model in Equation (1). Spatially, the INCA dataset primarily covers Austria and its surrounding regions, focusing particularly on the areas with complex terrain, such as the Alpine region [104]. The dataset has been evaluated in several studies [104,105]. In particular, air temperature data was shown to have high accuracy, making it a reliable parameter. Wind data, while generally accurate, has displayed some discrepancies, especially in complex alpine terrains. For

urban applications, which are the focus of this study, INCA thus represents a robust dataset with sufficient accuracy to support our methodology.

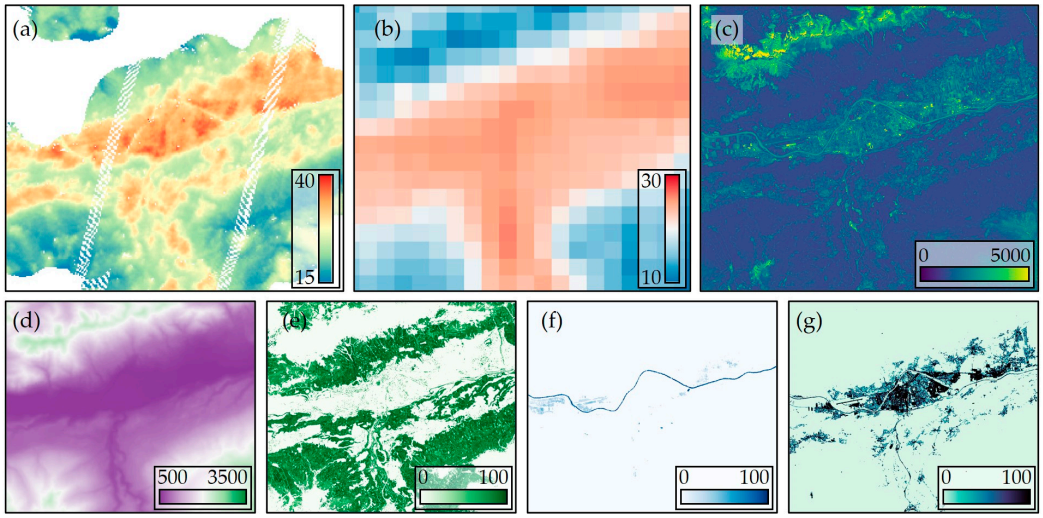

Figure 2. Overview of the datasets used in the training, shown for AREA I. The datasets are displayed in their native resolution. (**a**) ECOSTRESS LST in °C after masking by the quality control layer; see Section 2.4.1 for more details on masking (date and time of observation: 13 June 2023, 12:40:05, resolution 70 m). Data gaps due to clouds and instrument artifacts are visible. (**b**) INCA air temperature in °C (date and time of observation: 13 June 2023, 13:00:00, resolution 1 km). The image represents the closest INCA observation to the ECOSTRESS observation shown in (**a**). (**c**) Sentinel-2 band B4 reflectance (date and time of observation: 15 July 2023, 10:16:01, resolution 10 m). The image represents the cloud-free observation with all valid pixels closest to the ECOSTRESS observation shown in (**a**). (**d**) Digital elevation model (resolution 25 m). (**e**) Tree cover density. (**f**) Water and wetness index. (**g**) Imperviousness. The datasets (**e**–**g**) are from the reference year 2018, and they are shown in 10 m resolution.

Within our data processing workflow, we select the time window of interest, as specified in Section 2.1, and acquire the full spatial INCA dataset on an hourly resolution via an automated download directly from the GeoSphere Austria Data Hub [106].

2.3.3. Sentinel-2

The high-resolution input data for the LST mapping consists of the Sentinel-2 satellite data of the European Copernicus Earth observation program [45]. The Sentinel-2 mission provides high-resolution multispectral imagery, with spectral bands ranging from the visible to infrared part of the spectrum. Having a decametric resolution and a 5-day revisit time [45], the Sentinel-2 mission accurately captures the reflectance properties of surfaces around the time window of interest. It thus provides spatial information similar to, and more comprehensive than, the Bowen ratio parameter required in the physical model in Equation (1). This makes it a crucial input for our model, enhancing its capability to analyze and interpret surface characteristics and providing a link between LST and the various land cover classes.

For our data processing workflow, we select the Sentinel-2 images covering the area and time window of interest, and retrieve them locally from the Sentinel-2 Cloud Storage bucket [107]. We consider six spectral bands for the input (B2: Blue, B3: Green, B4: Red, B8: Near-Infrared, B11 and B12: shortwave infrared), as well as the Scene Classification Layer (SCL) for the identification of clouds and shadow. Instead of explicitly deriving spectral indices, such as normalized difference vegetation index (which is a combination of bands B4 and B8), we provide these raw bands directly to the model. This approach avoids explicit feature engineering and enables the model to identify optimal patterns

and combinations of input features autonomously during training. Sentinel-2 imagery is divided into standardized 100 km × 100 km tiles. AREA I and AREA II considered in our study are covered by the tiles 32TPT and 33UWP, respectively, with each tile having the projection of the 32 or 33 Universal Transverse Mercator (UTM) zone, respectively (UTM/WGS84 projection). An example Sentinel-2 B4 observation is shown in Figure 2c.

2.3.4. Additional Input Datasets

In addition to the Sentinel-2 satellite imagery and the INCA meteorological data, in our approach we utilize several supplementary numerical datasets to enhance the robustness and the accuracy of the model. These include the European Digital Elevation Model (EU-DEM) and derived parameters (slope, aspect), which provide detailed topographical characteristics [108], and several land cover datasets provided by the Copernicus Land Monitoring Service [109]:

(i) Tree cover density—a dataset which provides insights into vegetation distribution;
(ii) Water and wetness index—a dataset which indicates moisture levels and the presence of water bodies;
(iii) Imperviousness—a dataset which highlights the areas covered by artificial surfaces such as roads and buildings.

All the additional datasets are shown in Figure 2d–g. Combining these various additional layers with the optical and meteorological data accounts for environmental and land surface characteristics, thereby improving the overall modeling capability of our approach, and providing a link between LST and surface properties.

2.4. Methodology

After collecting the thermal and the optical remote sensing datasets, our gap-filling methodology is carried out in several major processing steps, which are summarized by a flowchart in Figure 3. These steps can be roughly divided into three parts: image processing (including preprocessing, observation matching, and further processing into input patches for the CNN model), CNN model training, and model assessment and evaluation.

2.4.1. Image Preprocessing

ECOSTRESS: The downloaded ECOSTRESS swath data are transformed into gridded single-band images in the UTM projection using the open-source *swath2grid* conversion algorithm [110]. In particular, we extract the LST and the quality control (QC) layers. The georeferenced LST layer is passed through several quality assessments and artifact mitigation steps. First, we make use of the intrinsic QC layer to mask out any low-quality pixels. The QC unsigned 16-bit data are stored as bit flags in the layer, with flags related to data quality, cloud, Temperature and Emissivity Separation algorithm diagnostics, and error estimates [101]. For the purposes of this study, we mask the LST layer by keeping only the best quality, cloud-free pixels, corresponding to the value for QC bits 1 and 0 = 00. This step is generally sufficient to eliminate most artifacts and clouds appearing in the observations. Second, we perform further manual checks to evaluate (i) the accuracy of georeferencing, and (ii) the quality of the QC masking. (i) In the case of a georeferencing offset of more than 50 m, the image is labeled as incorrect and discarded from further analysis. (ii) In the case of insufficient cloud masking (identified by extremely low negative temperatures), custom additional masking is performed.

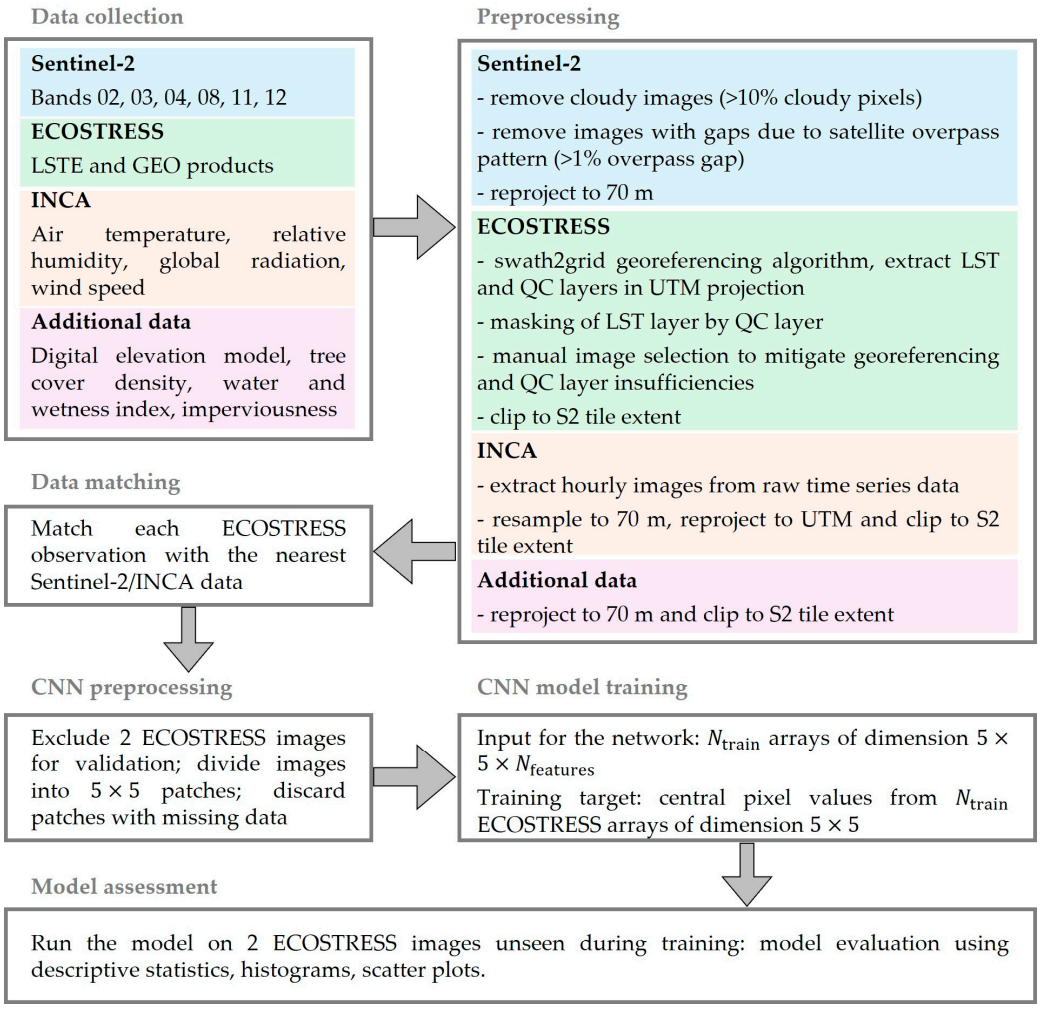

Figure 3. A flowchart outlining the main components of the LST gap-filling methodology: data collection, image processing (including preprocessing, data matching, and processing into input for CNN), CNN model training, and model assessment.

The LST dataset obtained after filtering suffers minimal issues due to incorrect georeferencing and undetected cloud coverage. As a result of the filtering, the data availability is reduced, leading to aperiodic availability of observations, and a typical 2–5-day revisit period in a specific location. The filtered ECOSTRESS LST data comprises the final dataset supplied to our model as the target values.

INCA: From the raw downloaded INCA time series data, we extract the observations which are temporally closest to the prepared ECOSTRESS LST, such that each extracted INCA observation corresponds to a single ECOSTRESS LST observation. The extracted images are resampled to the native ECOSTRESS resolution (70 m). Although such resampling does not add new information, it helps to smooth the images and facilitates a more systematic comparison with the ECOSTRESS data.

We note that the INCA data are provided at a much coarser resolution than ECOSTRESS (1 km compared to 70 m resolution). However, in the context of LST modeling, this represents a sufficient input, as meteorological conditions are less spatially heterogeneous than the land surface characteristics. On the other hand, nearly exact temporal matching is possible, due to the high hourly temporal resolution of the INCA dataset. As such, the INCA dataset meets our goal of relating the LST to the dynamic meteorological conditions at the time of the LST image acquisition.

Sentinel-2: As the input for our model, from the downloaded Sentinel-2 data we select and keep only the best available scenes, focusing on (i) mitigating cloud contamination and (ii) reducing data gaps due to swath overpass patterns, as the presence of any such low-quality areas in an image can negatively impact model training. To that end, we remove any of the images for which the metadata information indicates more than 10% of cloud coverage. Additionally, we discard all the observations that contain more than 1% data gaps. Such filtering leads to, on average, 2–4 scenes available per tile and per summer.

Even though the filtering described above leads to a modest final number of total observations per tile, for the purposes of our analysis this is an adequate input. More specifically, these filtered images are a good representation of the average surface reflectance properties for the time window around which they were taken. As such, they are deemed sufficient to meet our goal of relating the LST to the more static surface properties, such as the land cover.

Additional datasets: The additional datasets introduced in Section 2.3.4 are resampled to the native ECOSTRESS resolution.

As a final step in data preprocessing, we perform spatial and temporal image matching in several steps. (i) We resample (average) the Sentinel-2 images to the ECOSTRESS native resolution (70 m), (ii) we reproject ECOSTRESS, INCA, and additional datasets to the UTM projections, (iii) we clip ECOSTRESS/INCA/additional datasets to the Sentinel-2 tile extent, and (iv) we match every ECOSTRESS/INCA tiled observation to the temporally closest Sentinel-2 observation. The resampling, reprojection, and image clipping operations are performed using GDAL 3.7.0.

2.4.2. Preparation of the Input Patches for the CNN Model

The input to the CNN consists of 17 input features, described in Sections 2.3.2–2.3.4 and summarized in Table 2, spatially limited to a narrow image window (patch) around the pixel of interest. Adapting the approach in [92,111], we select a patch of size 5×5 as the input image to the CNN. At the native resolution of ECOSTRESS (70 m), this corresponds to a window of 350 m $\times$ 350 m, incorporating the contextual information surrounding each pixel. This inclusion of surrounding prominent features—such as vegetation, water bodies, agricultural fields, and industrial areas—enhances the model's ability to utilize and leverage contextual data during training.

Table 2. List of input features for the CNN.

Dataset	Input Features
INCA	air temperature, relative humidity, global radiation, wind speed in x direction, wind speed in y direction
Sentinel-2	bands B2, B3, B4, B8, B11, B12
EU-DEM	elevation, aspect, slope
Land cover	tree cover density, water and wetness index, imperviousness

Several steps are necessary to transform the images, prepared as described in Section 2.4.1, into the image patches provided as the input to the CNN. First, we generate 5×5 patches from all the images. For this, a sliding window of size 5×5 is applied, such that each pixel appears in a single patch only. Second, for patches corresponding to the ECOSTRESS data, we extract the value of the central pixel in each patch to serve as the target value for training. Third, we filter the patches, keeping only those that meet the following criteria: (i) all pixels across all input features have valid values and (ii) the ECOSTRESS value for the central pixel is valid. This step eliminates patches with missing data in the ECOSTRESS images [as visible, e.g., in Figure 2a], as well as patches with cloudy

or shadowy pixels in the Sentinel-2 images, identified using the SCL. The input for the CNN is thus a multidimensional array of shape $N_{\text{train}} \times 5 \times 5 \times N_{\text{features}}$, where N_{train} denotes the total number of filtered patches across all summer observations considered for the training, and $N_{\text{features}} = 17$ is the number of input features.

2.4.3. CNN Architecture for Pixelwise Regression

We utilize a standard CNN model to perform pixelwise LST estimation. The CNN is trained through supervised learning using Keras 2.13.1. Our model is adapted from the CNN configurations presented in [92,111], where a CNN architecture is developed for pixelwise segmentation and classification of Sentinel-2 imagery. Building upon this foundation, we have modified the architecture to address a continuous regression problem, enabling LST estimation.

The model architecture is shown schematically in Figure 4. We consider a network configuration consisting of a sequence of four two-dimensional convolutional layers. Each layer performs a convolution with a 2×2 kernel and a stride of 1×1, using the rectifier activation function (ReLU) between layers. The stability and the performance of the model are enhanced by batch normalization layers incorporated after the second and the fourth convolutional layers [112]. Overfitting is mitigated by a subsequent dropout layer [113], which excludes 10% of the neurons during training. The final regression is performed via a fully connected dense layer. The output layer has a size of 1, utilizing linear activation to produce an output value that corresponds to the LST prediction for the central pixel in a patch. The network architecture and the relevant hyperparameters are summarized in Table 3.

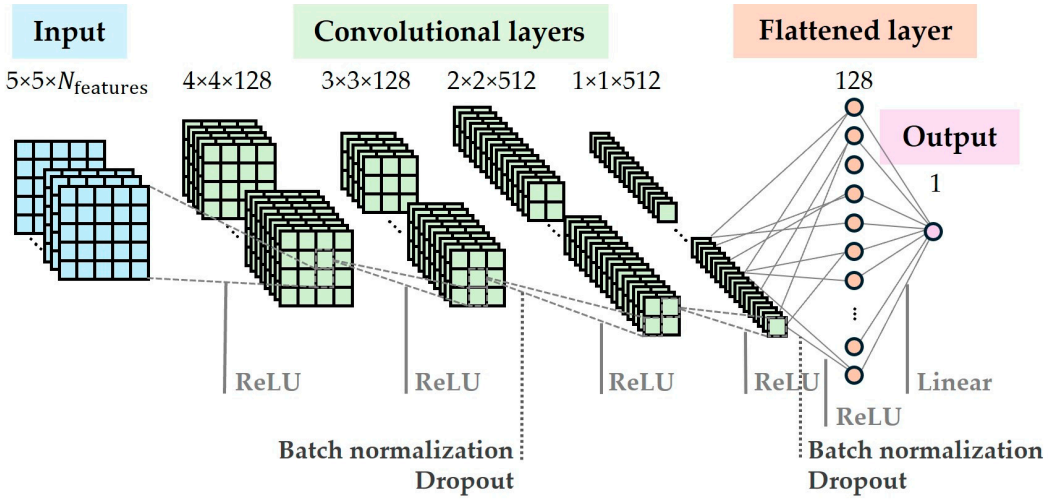

Figure 4. Scheme of the CNN architecture used for the LST gap-filling methodology.

The training dataset consists of nearly all summer observations. One observation per year and per area of interest is excluded from the training dataset and used as the test dataset to evaluate the model's performance after training. The ECOSTRESS data, detailed in Section 2.3.1, serves as the target data. Note that we leave out only very few observations from the training dataset for testing because the amount of available ECOSTRESS data is not abundant in terms of time (only a few observations available per week) and a scarcity of training data can possibly have detrimental effects on the model (the less the training data, the higher the risk that the model does not generalize well). For each area of interest, the training is carried out over the entire corresponding Sentinel-2 tile, namely, tile 32TPT for AREA I and tile 33UWP for AREA II.

Table 3. Summary of the CNN architecture and hyperparameters.

Input layer	size: 5 × 5 × 17
Convolutional layers	kernel size: 2 × 2; stride: 1 × 1; filters: 128 (layers 1 and 2), 512 (layers 3 and 4)
Dense layer	size: 128
Activation functions	rectified linear unit ('ReLU'), for the final layer 'linear'
Optimizer	adam (with inverse time decay), learning rate schedule: initial_lr = 0.001, decay_rate = 1, steps = 1000 × number_samples/batch_size
Loss function	mean absolute error
Number of epochs	50
Batch size	512
Train/validation split	80:20
Dropout rate	0.1

3. Results

3.1. Model Training

During the training phase, the input data is rescaled in the range [0, 1] using the min–max scaling. The N_{train} input data points are randomly shuffled into the training and validation datasets (used to evaluate the model's performance during training), with the split ratio being 0.2. The configuration of the CNN and the hyperparameters used during training are outlined in Table 3. Training is performed for 50 epochs, with patches processed in batches of size 512. We utilize Adam stochastic optimization with inverse time decay, starting with an initial learning rate of 0.0001, which decays by a factor of 1 every 1000 × (N_{train}/512) steps. The model is optimized using the mean absolute error (MAE) as the loss function

$$\text{MAE} = \frac{1}{N_{\text{train}}} \sum_{n=1}^{N_{\text{train}}} \left| \widehat{T_n} - T_n \right|, \tag{2}$$

with $\widehat{T_n}$ and T_n representing the predicted and true LST value for the central pixel in each patch, respectively.

Once model training is completed, the LST prediction is carried out over the unseen image in the test dataset. The test data is prepared in the same manner as described in Section 2.4.2, with the key difference being the use of a 1 × 1 sliding window to generate 5 × 5 patches for all non-border pixels in the image. This approach facilitates pixelwise predictions, allowing the creation of output images in a raster format that matches the resolution of the input images.

3.2. Performance Evaluation

We assess the model and its generalization capabilities by generating the LST predictions on the test dataset consisting of the images unseen by the model. More precisely, no pixel patches belonging to the test dataset were provided to the CNN for the training. These predictions are compared with the corresponding ECOSTRESS observations to evaluate the performance.

It is important to highlight a key distinction between the generation of the test and validation datasets. The validation dataset is a subset of filtered pixel patches derived from the train/validation split. In contrast, the test dataset is created by excluding an entire image before the train/validation split. The validation dataset is thus less distinct

from the training dataset than the test dataset. As a result, predictive performance of the model on the test data provides a more accurate indication of the model's generalization ability compared to the validation data. This is particularly relevant for assessing the model's extrapolation capabilities, where "extrapolation" refers to making predictions on data points that fall outside the range of the training data, such as predicting LST in high-temperature scenarios with the model trained on lower-temperature observations.

For a more comprehensive analysis, we assess the model over different training datasets by varying the hour range of the observations chosen for the training. Therefore, besides using training datasets with observations spanning the entire day, we also consider training datasets limited to smaller hour ranges at different times of the day, for example ranges falling in the morning or in the afternoon.

3.3. Qualitative Analysis of the Predictions

We begin by conducting a visual evaluation of the model predictions. In this qualitative assessment, the results are generally promising, as the model predictions closely resemble the ECOSTRESS measurements (see Figure 5 for examples of predictions over AREA I and AREA II). While some visual discrepancies do occur, they are typically limited to small, isolated patches of pixels, which constitute a minor portion of the overall image and are usually located outside of urban areas. These artifacts may originate from occasional model errors or input data issues (e.g., cloud interference). Despite this, the model predictions effectively capture the spatial features present in the ECOSTRESS observations, often further enhancing spatial detail by increasing contrast—particularly noticeable in features like rivers (cf. ECOSTRESS observations and the corresponding model predictions in Figure 5). The improvement in spatial detail is largely due to the integration of higher-resolution input data, which provides additional fine-scale information.

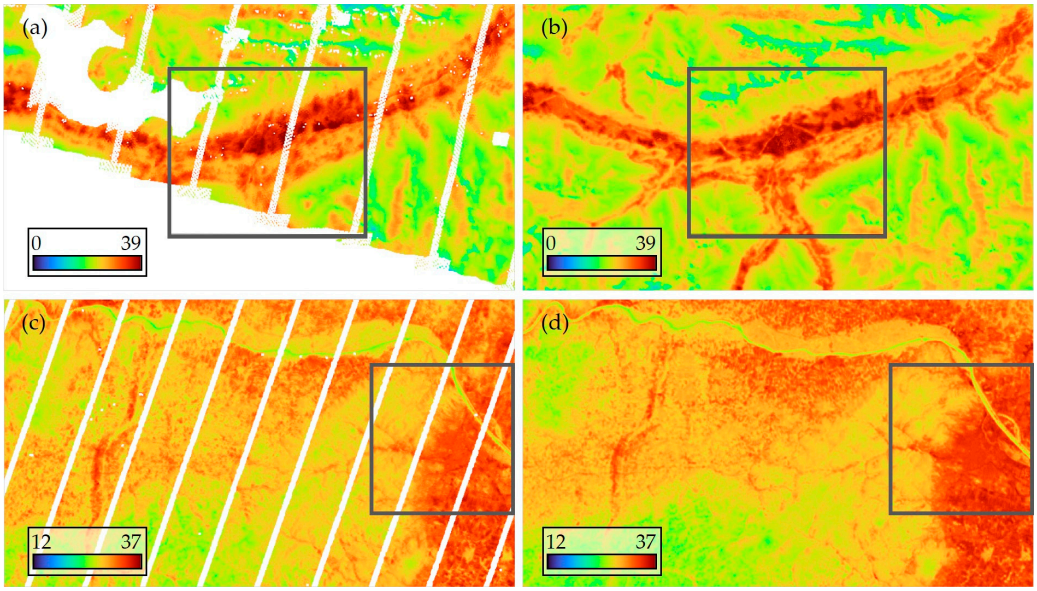

Figure 5. Comparison between LST ECOSTRESS measurements and model predictions in °C. The images display LST data for two areas of interest, outlined by a bounding box in each image. (**a**) Masked ECOSTRESS measurement and (**b**) corresponding model prediction for AREA I. Date and time of observation: 12 June 2022, 13:26:01. (**c**) Masked ECOSTRESS measurement and (**d**) corresponding LST prediction over AREA II. Date and time of observation: 4 August 2022, 16:31:34.

Additionally, the model exhibits a strong ability to fill various gaps in the ECOSTRESS observations, including those caused by cloud cover, image border limitations, and grid-pattern sensor artifacts. These gaps, visible in Figure 5a,c, are effectively addressed by the

model, as shown in Figure 5b,d. A close-up of typical ECOSTRESS grid artifacts is shown in Figure 6a, and the corresponding correction by the model, as well as the enhancement of spatial detail, is demonstrated in Figure 6b.

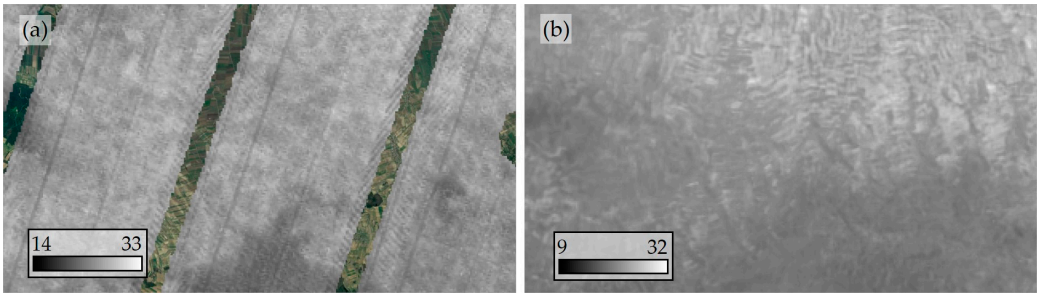

Figure 6. (**a**) Close-up of grid artifacts in ECOSTRESS LST observation, shown in grayscale to enhance visibility. (**b**) The corresponding model prediction corrects the artifacts and increases spatial details. (Location: WGS84 coordinates 48.65398°N, 16.31361°E. Observation date and time: 4 June 2022, 16:39:50).

Overall, the visual analysis shows that the model not only replicates the spatial features of ECOSTRESS observations, but it also enhances detail and effectively fills various gaps appearing in the observations. These strengths highlight the model's potential for addressing common issues in remote sensing datasets and improving the accuracy of LST predictions.

3.4. Quantitative Analysis of the Predictions

For the statistical analysis, we consider all the pixelwise LST pairs, consisting of the prediction value and the corresponding ECOSTRESS measurement, within a single Sentinel-2 tile. To ensure valid comparisons, we include only the pairs where both pixels contain valid data. In particular, predictions for pixels lacking valid ECOSTRESS observation data (e.g., due to QC masking) are excluded from the analysis. The set of N valid pixels for a given tile and observation considered in the analysis is denoted as $\mathcal{P}$. Each prediction is evaluated based on the pixel prediction error $\Delta_p = \widehat{T_p} - T_p$, where T_p and $\widehat{T_p}$ are the true (ECOSTRESS) and predicted LST for a single pixel $p \in \mathcal{P}$, respectively. The following statistics are subsequently derived to analyze the pixelwise prediction error distribution within a tile: (i) mean error (ME), defined as $ME = \sum_{p\in\mathcal{P}} \Delta_p / N$, and mean absolute error (MAE), defined as $MAE = \sum_{p\in\mathcal{P}} |\Delta_p| / N$ [cf. Equation (2)]; (ii) coefficient of determination r^2, given by

$$r^2 = 1 - \frac{\sum_{p\in\mathcal{P}} \Delta_p^2}{\sum_{p\in\mathcal{P}} \left(\overline{T} - T_p\right)^2}, \tag{3}$$

where $\overline{T} = \sum_{p\in\mathcal{P}} T_p / \mathrm{N}$ is the mean value of the true LST for all pixels $p \in \mathcal{P}$; (iii) minimum (min) and maximum (max) value of the prediction error; (iv) standard deviation (std) of the prediction error; and (v) percentiles of the prediction error.

In our focus on urban applications, we prioritize the MAE—the metric we used as the loss function during training—as the key statistic for validating the predictions. While the maximum acceptable MAE varies depending on the specific application, a general guideline is that the MAE should not exceed 3 °C, with no more than 25% of the pixelwise absolute error above this threshold. This standard aligns with recent studies investigating various machine learning approaches for estimating LST [93], as well as a milestone survey referenced therein [99].

Additionally, we consider the r^2 score defined in Equation (3). This is a scale-independent metric that indicates how well a model fits data, with its values ranging from $-\infty$ to 1. The larger the value, the better the fit. The maximum value of 1 is achieved

if and only if all the prediction errors vanish, indicating a perfect fit. Negative values indicate that the model fits the data worse than a simple baseline prediction given by the mean value of the data. Such baseline prediction has $r^2 = 0$, as one can easily verify from Equation (3). While r^2 is a valuable metric for model evaluation, it can be challenging to correctly interpret in isolation. In fact, a high r^2 value can be a sign of a bad model which overfits the data and is not capable of generalizing adequately. In general, acceptable r^2 values depend on the data variability and how much of this variability is due to the noise in the data, rather than the underlying signal. While there is no universal standard for acceptable r^2 values in LST modeling, remote sensing studies typically consider values above 0.5–0.7 as acceptable, with a preference for higher values up to 0.9–0.95, above which the chance of overfitting increases. Note that there is no direct relationship between MAE and r^2; low MAE can coexist with low r^2, and vice versa. Finally, to ensure a comprehensive analysis, we also include the minimum, maximum, standard deviation, and percentiles of the prediction errors, which provide a more complete picture of model performance.

A total of 22 image predictions on test data are computed and evaluated. Table 4 summarizes the statistics for the individual predictions with the four best and four worst resulting MAE, as well as the ensemble statistics of the 22 predictions. The columns denoting the 10th, 15th, 85th, and 90th percentile are labeled as *10p*, *15p*, *85p*, and *90p*, respectively. All predictions are generated for ECOSTRESS observations unseen during training, with the time of observation indicated in the column *Date and time*, and the fraction of valid pixels in the observation for which the statistics are calculated (e.g., pixels unmasked by the ECOSTRESS QC mask) indicated in the column *valid*. Note that the predictions are not all derived from the exact same trained model. Instead, they are derived from different realizations of the model yielded by training on observations spanning different hour ranges (as discussed in Section 3.2). The time range used for training the corresponding model is indicated in the column *hour range*.

The bottom row in each tile cell displays ensemble statistics computed for all the valid pixels across all 22 predictions. The ensemble statistics provide a comprehensive assessment of the model's overall predictive performance, as opposed to evaluating individual predictions based on specific datasets or single training instances. It is important to highlight that the ensemble MAE represents the average of the single prediction MAEs weighted on their pixel count. However, this statement does not apply to r^2 and percentiles.

As shown in Table 4, the ensemble MAE for tile 32TPT is 1.93 °C, with the 10th and 90th percentiles at −2.59 °C and +3.16 °C, respectively. The ensemble MAE for tile 33UWP is 1.60 °C, with the 10th and 90th percentiles at −2.68 °C and +2.27 °C, respectively. This means that at least 80% of the pixel errors fall within the ±3 °C range, with only a slight deviation for the 90th percentile in 32TPT. The slightly worse performance over the 32TPT tile could reflect the more complex microclimate and surface conditions of the alpine environment in AREA I, which increases variability in the temperature data and leads to a broader error distribution. In contrast, the flatter urbanized conditions in AREA II lead to more stable LST patterns, resulting in a narrower error range. Despite this, the error margins in both locations fall well within acceptable limits. Additionally, the ensemble r^2 values of 0.87 for both tiles indicate a robust overall fit and a strong correlation between the model predictions and the ECOSTRESS data, despite some individual predictions having lower r^2. Note that having a few individual predictions with low r^2 can be expected because, on one hand, noise and errors can particularly impact r^2 for individual observations and, on the other hand, as the ECOSTRESS training data are (temporally) scarce, there can be specific conditions under which the model performance is more limited.

Table 4. Statistics for the error distributions of 22 model predictions on tiles 32TPT and 33UWP, showing the four best and four worst predictions based on mean absolute error (MAE). Predictions are made on unseen ECOSTRESS observations. All metrics are reported in °C, except r^2, which is dimensionless. Column labels are defined in the main text.

32TPT												
Date and time	**Hour range**	**MAE**	**ME**	r^2	**min**	**max**	**10p**	**15p**	**85p**	**90p**	**std**	**valid**
16 August 2023, 11:38:45	11:00–15:00	1.01	0.0	0.81	−24.32	30.05	−1.49	−1.18	0.93	1.28	1.79	0.59
4 August 2022, 13:17:00	13:00–19:00	1.44	−0.99	0.66	−12.5	27.14	−2.88	−2.48	0.42	0.76	1.62	0.27
13 June 2023, 12:40:05	11:00–15:00	1.56	−0.02	0.78	−12.2	25.62	−2.52	−1.96	1.81	2.31	2.15	0.48
21 August 2022, 05:57:47	04:00–11:00	1.6	0.51	0.68	−13.92	50.95	−1.78	−1.32	2.39	3.06	2.16	0.77
8 June 2023, 15:08:57	13:00–19:00	2.73	−1.35	0.79	−17.65	21.07	−5.64	−4.85	1.67	2.34	3.28	0.13
22 July 2023, 17:13:37	00:00–23:00	2.97	2.08	−0.27	−27.62	98.1	−1.35	−0.43	3.83	4.56	4.68	0.3
19 August 2023, 06:01:12	03:00–07:00	3.09	0.02	0.23	−49.21	41.42	−4.16	−3.22	3.89	4.74	4.49	0.21
19 August 2023, 06:01:12	00:00–23:00	3.67	−2.35	−0.02	−50.53	51.82	−7.02	−5.83	1.59	2.53	4.62	0.21
Ensemble statistics	-	1.93	0.36	0.87	−50.53	98.1	−2.59	−1.94	2.62	3.16	2.71	0.54
33UWP												
Date and time	**Hour range**	**MAE**	**ME**	r^2	**min**	**max**	**10p**	**15p**	**85p**	**90p**	**std**	**valid**
2 July 2022, 5:26:25	00:00–23:00	0.85	−0.14	0.46	−6.81	28.6	−1.43	−1.16	0.74	1.04	1.38	0.62
2 July 2022, 5:26:25	03:00–07:00	0.98	−0.46	0.49	−5.69	25.87	−1.83	−1.58	0.65	0.92	1.27	0.62
15 August 2023, 07:36:45	04:00–11:00	1.1	0.0	0.69	−7.39	8.05	−1.77	−1.4	1.38	1.74	1.43	0.66
2 July 2022, 5:26:25	04:00–11:00	1.1	0.03	−0.13	−16.65	56.41	−1.65	−1.37	1.23	1.56	2.01	0.62
16 August 2022, 11:38:39	00:00–23:00	2.18	−0.72	0.81	−20.24	17.37	−4.45	−3.42	1.85	2.41	2.97	0.41
12 August 2023, 13:13:33	07:00–11:00	2.26	−0.65	−0.15	−13.32	62.62	−3.9	−3.35	1.98	3.06	2.84	0.24
18 June 2023, 10:13:08	00:00–23:00	2.55	−2.14	0.4	−17.4	7.81	−5.7	−4.88	0.27	0.72	2.59	0.53
18 June 2023, 10:13:08	00:00–23:00	2.61	−2.39	0.4	−17.34	62.68	−5.59	−4.81	−0.21	0.33	2.33	0.53
Ensemble statistics	-	1.6	−0.15	0.87	−33.14	135.46	−2.68	−2.08	1.78	2.27	2.22	0.59

Finally, it is important to note that the maximum overestimation and underestimation errors at individual pixels can occasionally reach extreme values, with some predicted temperatures falling outside reasonable ranges (refer to the *max* and *min* columns in Table 4). Such errors are primarily outliers; they correspond to the artifacts reported in the qualitative analysis in Section 3.3 and have a limited impact on overall predictive performance. They could be mitigated through targeted postprocessing techniques, ensemble learning (i.e., combining predictions from multiple models), or by flagging these data points as invalid.

Figure 7 provides further analysis of the LST distributions for the two prediction ensembles, displayed through histograms and bivariate histograms. Panels (a) and (c) compare the predicted with observed LST distributions for tiles 32TPT and 33UWP, respectively. While the two datasets do not align perfectly, the model generally captures the major temperature peaks in terms of both width and height, indicating reasonable agreement. The bivariate histograms in panels (b) and (d) further reveal the relationship between the predicted and the true LST values in 33TPT and 33UWP, respectively. Most data points fall along the diagonal, confirming strong overall agreement, though some outliers are present. These deviations may originate from systemic data issues such as unmasked clouds (thin linear artifacts in the histograms), or from the model's tendency to overestimate low LST values in alpine areas [a larger concentration of outliers present in panel (b)].

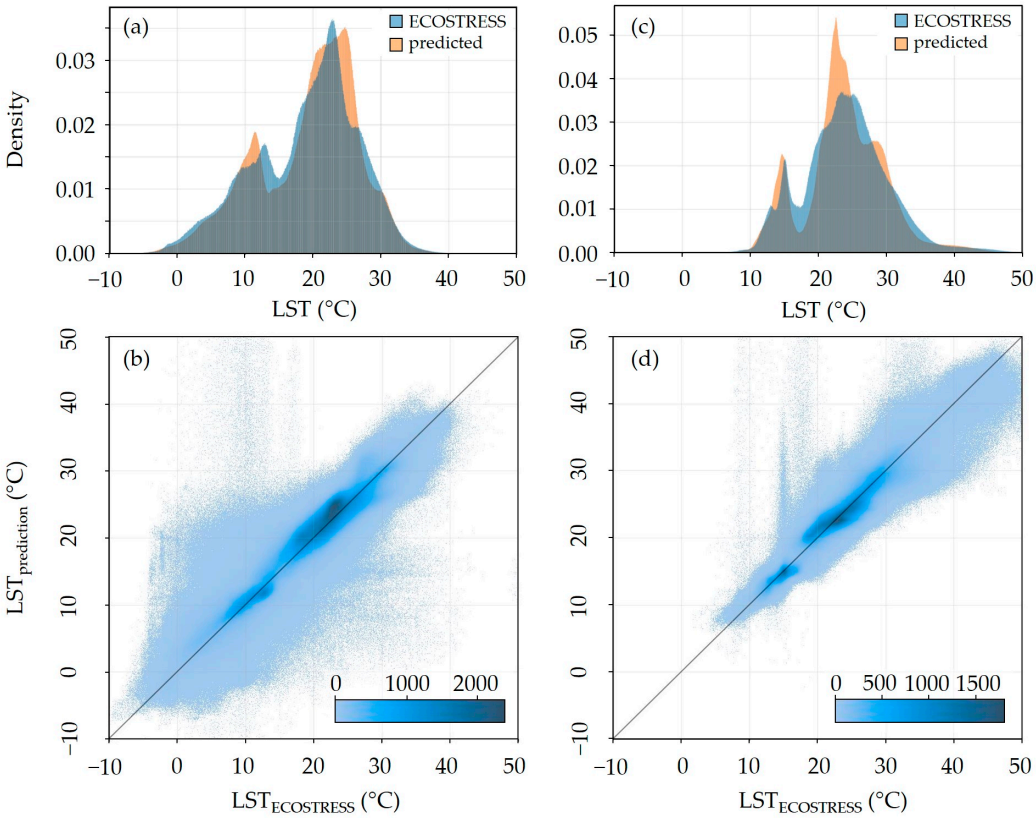

Figure 7. Histograms for the disjoint (above) and joint (below) distribution of LST for all pixels across all the predictions considered in Table 4. The colored bars in the bivariate histograms indicate pixel count. (**a**,**b**) Results for tile 32TPT; the MAE and r^2 are, respectively, 1.93 °C and 0.87. (**c**,**d**) Results for tile 33UWP; the MAE and r^2 are, respectively, 1.6 °C and 0.87.

We considered models trained on different time windows to derive the 22 predictions evaluated in Table 4. In particular, we considered full-day and afternoon models trained on observations spanning, respectively, the entire day and afternoon hours. To assess the impact of the training data time window on the model performance, in Table 5 we compare the ensemble statistics for the predictions which are derived from the full-day model with those derived from afternoon models. While the MAE is slightly lower for the afternoon models, the r^2 values are similar. This indicates that the full-day model is less accurate than the afternoon model, while they explain data variability equally well. However, the error distribution for the full-day model is significantly more spread, with higher maximum overestimation and underestimation errors. In fact, the full-day model mostly contributes to the lower performance metrics in Table 4. Despite having more data for training, the full-day model thus performs worse overall than the narrower afternoon

model. This is likely a sign that the relationship between the considered input features (e.g., air temperature, etc.) and LST changes with the time of the day. In fact, the input features include only atmospheric conditions at a single point in time, whereas time series data are likely to determine the LST.

Table 5. Ensemble statistics for the predictions of Table 4 that were derived from a full-day model or an afternoon model, grouped by model type and tile. All metrics are reported in °C, except r^2, which is dimensionless.

Model	MAE	ME	r^2	Min	Max	10p	15p	85p	90p	Std	Valid
32TPT, full day	2.16	−0.04	0.82	−50.53	98.1	−3.41	−2.69	2.48	3.04	3.09	0.55
32TPT, afternoon	1.96	1.06	0.81	−27.3	27.14	−1.56	−0.92	3.02	3.47	2.29	0.48
33UWP, full day	1.79	−0.25	0.85	−33.14	135.46	−3.17	−2.48	1.86	2.38	2.51	0.58
33UWP, afternoon	1.39	−0.19	0.73	−9.71	10.44	−2.4	−1.94	1.58	2.06	1.77	0.61

For completeness, in Figure 8 we display the LST distributions for the afternoon model prediction ensembles for tiles 32TPT and 33UWP, which can be directly compared with Figure 7. The histograms in panels (a) and (c) show a similarly reasonable agreement, as seen in Figure 7, with the morning-related lower temperature peaks now absent. The bivariate histograms in panels (b) and (d) demonstrate improved correlation and fewer outliers, indicating a stronger alignment between predictions and observations compared to the full-day model prediction ensembles.

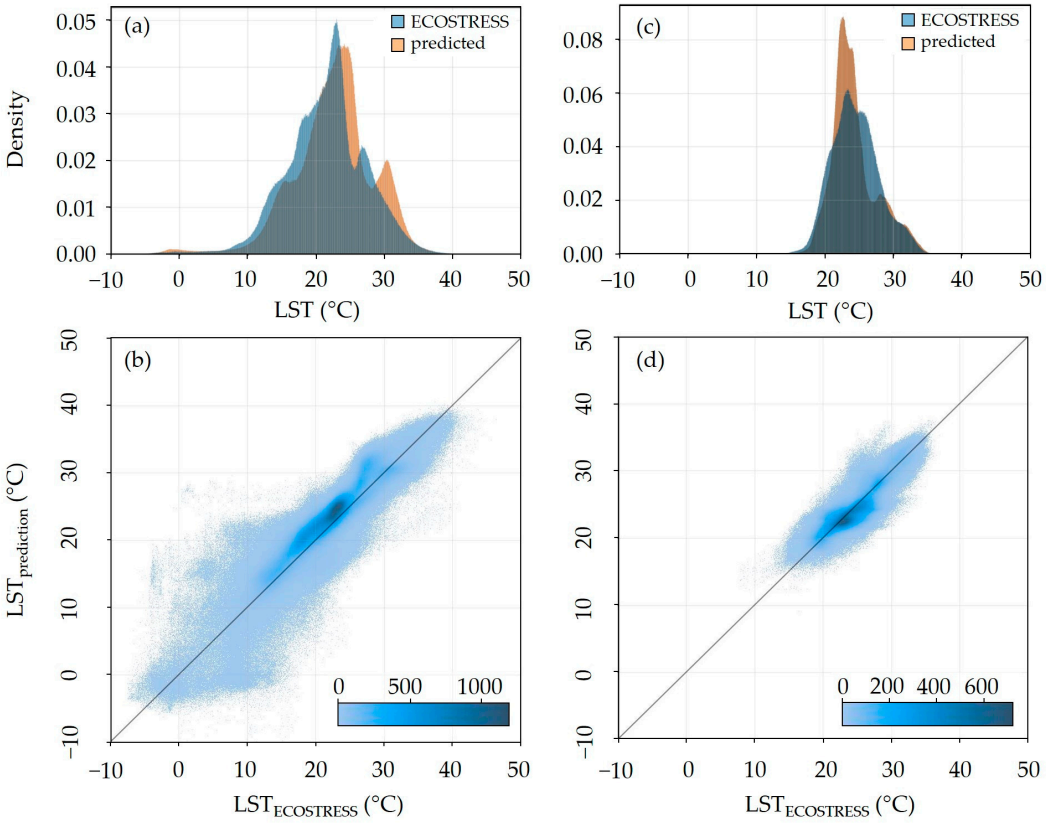

Figure 8. Histograms for the disjoint (above) and joint (below) distribution of the LST for all pixels across all afternoon model predictions considered in Table 4. The colored bars in the bivariate histograms indicate pixel count. (**a**,**b**) Results for tile 32TPT; the MAE and r^2 are, respectively, 1.96 °C and 0.81. (**c**,**d**) Results for tile 33UWP; the MAE and r^2 are, respectively, 1.39 °C and 0.73.

Note that the predictions considered so far were computed for the same tile on which the model was trained. Here, to robustly evaluate the spatial generalization capabilities of

the model, we consider predictions on Sentinel-2 tiles not seen during training. Specifically, we consider several predictions on tiles neighboring the training tiles. We opt for the validation on neighboring tiles because training and prediction should be performed on geographically similar regions. Otherwise, the model cannot be expected to behave well, as predicting on a geographically different area can result in spatial extrapolation that is too far from what the model learns. Table 6 summarizes the statistical evaluation of such predictions. As the table shows, the results are in line with the results of Table 4. We can thus conclude that the model spatially generalizes well. This also indicates that the model does not suffer from overfitting.

Table 6. Statistics for the error distributions of predictions generated on neighboring tiles. All metrics are reported in °C, except r^2, which is dimensionless.

Date and Time	Predict Tile	Train Tile	MAE	ME	r^2	Min	Max	10p	15p	85p	90p	Std	Valid
4 August 2022, 16:31:34	33UWP	33UVP	1.13	−0.7	0.7	−10.38	6.53	−2.52	−2.03	0.56	0.81	1.39	0.89
4 June 2022, 16:39:50	33UWP	33TWN	1.21	−0.38	0.57	−8.88	8.65	−2.62	−2.03	1.06	1.37	1.59	0.7
12 June 2022, 13:26:01	32TPT	32TQT	1.33	−1.01	0.77	−12.65	12.43	−2.69	−2.28	0.25	0.55	1.42	0.49
4 August 2022, 16:31:34	33UVP	33UWP	1.43	−1.04	0.48	−9.73	6.23	−2.9	−2.52	0.41	0.75	1.46	0.89
2 August 2023, 16:26:54	33UWP	33UVP	1.56	−0.04	0.4	−7.47	10.97	−2.5	−2.03	2	2.44	1.93	0.46
3 August 2022, 17:19:33	32TQT	32TPT	1.68	0.89	0.7	−23.23	20.03	−1.29	−0.78	2.83	3.34	2.04	0.89
8 June 2023, 15:08:57	32TPT	32TQT	3.15	−1.6	0.72	−64.92	24.07	−5.28	−4.62	1.47	2.66	3.7	0.13
Ensemble statistics	-	-	1.44	−0.39	0.84	−64.92	24.07	−2.66	−2.16	1.3	1.8	1.9	0.64

Finally, as all the predictions discussed so far are generated within the same temporal range as the training data, we also evaluate the model's performance when extrapolating beyond this range, such as generating morning predictions from afternoon models. The results are summarized in Table 7. The accuracy for these extrapolated predictions is significantly lower compared to interpolated ones. This is somewhat expected, given the inherent challenges of temporal extrapolation. Nonetheless, the statistics remain close to the acceptable bounds, with approximately 80% of the pixel errors falling within the ±5 °C range. This suggests a robust and consistent relationship between input features and LST, with minimal variations between morning and afternoon predictions. However, for more fine-scale modeling and improved accuracy, such extrapolation is not sufficient.

Table 7. Ensemble statistics for extrapolating morning predictions from afternoon models. All metrics are reported in °C, except r^2, which is dimensionless.

Model	MAE	ME	r^2	Min	Max	10p	15p	85p	90p	Std	Valid
32TPT, extrapolating predictions	3.12	−0.35	0.72	−52.81	56.51	−5.41	−4.28	3.42	4.33	4.14	0.55
33UWP, extrapolating predictions	2.96	0.28	0.64	−46.14	30.37	−4.67	−3.48	3.92	4.57	3.8	0.61

4. Discussion

4.1. Application of the Data Fusion Approach

In our proposed approach, we employ a CNN model for pixelwise LST predictions at moderate to high spatial resolution (i.e., 70 m) combining multi-source and multi-resolution input features (i.e., coarse resolution reanalysis data from a meteorological nowcasting

prediction system, high-resolution land cover data, high-resolution multi-spectral optical satellite data) to gap-fill and densify remote-sensing-based LST observations. The CNN model is trained based on the ECOSTRESS-LSTE L2 dataset provided via the NASA Earthdata portal. The model makes use of the 5 × 5 input pixel patches, corresponding to a 350 m × 350 m area at the native resolution of ECOSTRESS, incorporating surrounding contextual information such as vegetation cover and water bodies to enhance prediction accuracy. The advantage of the proposed methodology compared to conventional and purely remote sensing-based techniques is that the model-based approach combines the superior dense temporal sampling of the meteorological model data with the substantially higher spatial detail of the remote-sensing-based LST observations. Having such a model in place allows us to obtain dense LST estimates at a high spatial resolution to support a variety of applications like supporting local spatial planning authorities in identifying hotspot regions within urban environments, analyzing the context between land use and land cover and associated heat impact, or supporting the development of local, near-real-time heat stress warning systems by exchanging the reanalysis data with numerical weather prediction parameters, to name a few. Having such applications in mind, the prediction accuracy (i.e., observed r^2 and MAE) of our model is good, and allows us to highlight and analyze the spatial variability and temperature contrasts between various land cover types.

The advantage of our method compared to other approaches which purely rely on remote-sensing-based LST estimates and data cross-calibration (e.g., [59]) is two-fold. First, due to the strong diurnal variations in LST mainly depending on the meteorological conditions, fusing data from various satellite sensors to gap-fill LST data requires sophisticated inter-calibration techniques to correct for LST differences caused by different overpass times. Thus, using meteorological reanalysis data from a highly resolved numerical weather prediction (NWP) model with similar spatial resolution, like coarse resolution satellite-based LST estimates (e.g., Sentinel-3, MODIS, VIIRS), has the advantage of offering the meteorological conditions for any observation time and already incorporating a physical-based treatment of meteorological processes. Second, due to the superior temporal sampling of the NWP model outputs, our trained model can be applied to any time step and is less dependent on satellite flight schedules and revisit times, finally enabling us to create a more representative LST dataset which provides comparability between regions over large scales. Furthermore, the NWP output can also be replaced with the output from Regional Climate Models (RCMs) to analyze and evaluate future climate change impacts. Alternative approaches (e.g., [85]) make use of geostationary satellite imagery (e.g., MSG SEVIRI, GOES) to gap-fill LST data, which offers hourly or even sub-hourly temporal observations. Yet, they typically have a larger Ground Sample Distance (~5 km in mid-latitudes) than the above-mentioned polar-orbiting instruments (~1 km) and cannot be considered for the RCM approach in the context of climate change adaptation studies.

Other studies have successfully used multi-source data fusion to gap-fill LST by incorporating land surface models [77] and applying deep learning techniques to fuse remote sensing data with in situ observations [94]. These approaches have demonstrated high spatial and temporal coverage with strong accuracy over specific areas and time windows of interest. Our approach complements these efforts by introducing a lightweight CNN model that is robust across time domains, allowing us to generate LST predictions consistently over a 3-month summer period. This flexibility enables the creation of long-term, high-density LST datasets for any region with available meteorological data, facilitating the development of near-real-time LST monitoring systems that can be seamlessly implemented for real-time applications.

4.2. Limitations of the Deep Learning Model

While the model demonstrates generally good performance, there are several limitations that affect its accuracy and reliability. One of the main issues observed is the occurrence of over- and underestimation errors at individual pixels, as reflected in the minimum and maximum values in the ensemble statistics (see Table 4). Although these errors are infrequent, they contribute to outliers that can affect the model's overall predictive performance. Tracing the exact source of these errors is challenging due to the intricate relationships between input features—such as land cover, meteorological data, and satellite imagery—and LST, as well as the intrinsic complexities of deep-learning-based models. These errors could originate from the inherent variability in surface conditions (leading to a complex LST modeling response), from the inconsistencies in the input data (e.g., unmasked clouds, noise, and other artifacts), or from model architecture limitations. While the calculated ensemble MAEs for both tiles remain within acceptable limits, addressing these outliers could further enhance accuracy. Potential approaches that could help improve error management and provide a more robust and interpretable framework include tailored postprocessing techniques, ensemble learning, or hybrid models which incorporate additional physical constraints.

The performance of the model is also impacted when trained on the data spanning an entire day, as demonstrated by the comparison of the full-day and the afternoon ensemble statistics (see Table 5). Specifically, the full-day model tends to exhibit poorer performance compared to models trained on specific time ranges, such as afternoon-only datasets, despite having generally more data available for training. This difference is likely due to the dependency of the LST on the input features changing with the time of day, as more complex time series dynamics in such relationships are not considered in our model. Consequently, the full-day model exhibits a more spread error distribution, with higher maximum over- and underestimation errors. We speculate that the history of the solar radiation input might have a particular influence on this behavior, as for instance discussed in [114]. This is supported by the observed improved performance when only considering observations of a specific time of the day compared to the full day model.

Another limitation is the model's ability to generalize across temporal and spatial domains. Temporally, the model's performance is impacted when predictions are made outside the training time range. For example, morning predictions made by a model trained on afternoon data exhibit lower accuracy than interpolated predictions, suggesting that fine-scale modeling and improved accuracy for temporally extrapolated predictions would require training on time-specific data. Likewise, any out-of-season extrapolation would likely face similar limitations. This can be mitigated in future studies by training models on data corresponding to the specific season and conditions of interest [115,116]. Spatially, we observe that the model performs well when applied to unseen regions (see Table 6), which highlights the potential for spatial extrapolation. However, this level of generalization is limited to neighboring areas with similar characteristics to those used during training. For broader applications, regional robustness could be improved by training the model on a tile-by-tile basis or using data from multiple representative regions, enabling the model to learn a more diverse set of spatial patterns and new geographic areas.

An additional limitation stems from the scarcity and uneven quality of ECOSTRESS data available for training. The limited availability of good-quality observations affects the model's ability to generalize, particularly in cases where predictions are made outside of the training data time range. For instance, morning predictions from models trained on afternoon data show worse statistics than interpolated predictions, but they remain within acceptable limits. Extrapolation, in general, proves to be more error-prone than interpolation due to the model's inability to fully capture diurnal variations in LST.

4.3. ECOSTRESS Data Quality

We encountered several data quality issues when collecting the ECOSTRESS-LSTE data for both areas of interest. These issues are primarily observed in the form of missing data due to cloud contamination and artifacts and georeferencing inconsistencies, which can impact the reliability of the data. Applying the associated ECOSTRESS quality mask (provided by the QC layer in the ECOTRESS-LSTE dataset) helps mitigate some of these issues.

The quality issues affecting the ECOSTRESS dataset can be divided into three categories: (i) instrument artifacts, (ii) incorrect georeferencing, and (iii) QC layer insufficiencies. (i) Instrument artifacts are a prominent issue, appearing as stripes (linear or grid-like patterns disrupting data uniformity) and grooves (irregular indentations affecting data consistency), as illustrated in Figure 9a. These artifacts are caused by damage to the thermal infrared sensor during pre-launch testing [117]. They are an intrinsic property of the ECOSTRESS dataset, arising from issues in the sensor itself, and as such, they cannot be eliminated. However, as shown in the visual analysis in Section 3.3, the CNN model is able to correctly identify and mitigate these artifacts effectively (see, e.g., Figure 6). (ii) Another significant issue is inconsistent or incorrect georeferencing, as provided by the ECOSTRESS-GEO geolocation dataset within the *swath2grid* algorithm (see Section 2.3.1 for details). As illustrated in Figure 9a, incorrect georeferencing appears as misalignment between LST data and geographic coordinates, while inconsistent georeferencing refers to variability in spatial accuracy across different observations. This issue is sporadic and unpredictable, and developing an automated correction procedure is beyond the scope of this work. In our processing workflow, we addressed this by reviewing all observations in the training dataset and excluding those with inaccurate georeferencing from further analysis, as the accuracy of the deep learning model depends on the quality of the target data (i.e., ECOSTRESS LST). (iii) The original ECOSTRESS QC mask is intended to filter out unreliable data. However, it is not always sufficient and can introduce further complications, such as incorrect cloud masking, leading to erroneous temperature readings. Specifically, the QC mask occasionally failed to fully remove cloud cover, leading to unrealistic temperature gradients and misleading thermal readings due to partial cloud obstruction. An example of this issue is illustrated in Figure 9b,c, where a cloud is not correctly masked. To address this, we screened the QC data and added additional manual masking in observations with significant cloud masking artifacts.

Despite our efforts to mitigate ECOSTRESS data quality issues, some of the observed prediction artifacts (such as the significant under- or overestimation errors reported in Table 4) may still originate from undetected low-quality data used for the model training. Similar data filtering and quality issues with ECOSTRESS datasets have been reported in previous studies [117,118].

4.4. Future Directions

Planned future directions include efforts to enhance the spatial resolution of LST predictions, specifically by exploring techniques to downscale LST to 10 m resolution. This approach will explore the scaling effects characteristic of downscaling, reported in previous studies [59–62], as well as deep-learning-based methodologies to overcome these issues. A downscaled LST product provided at high temporal resolution and spatial coverage would provide more detailed insights, particularly in urban environments where fine-scale temperature variations are critical for local climate analysis and planning.

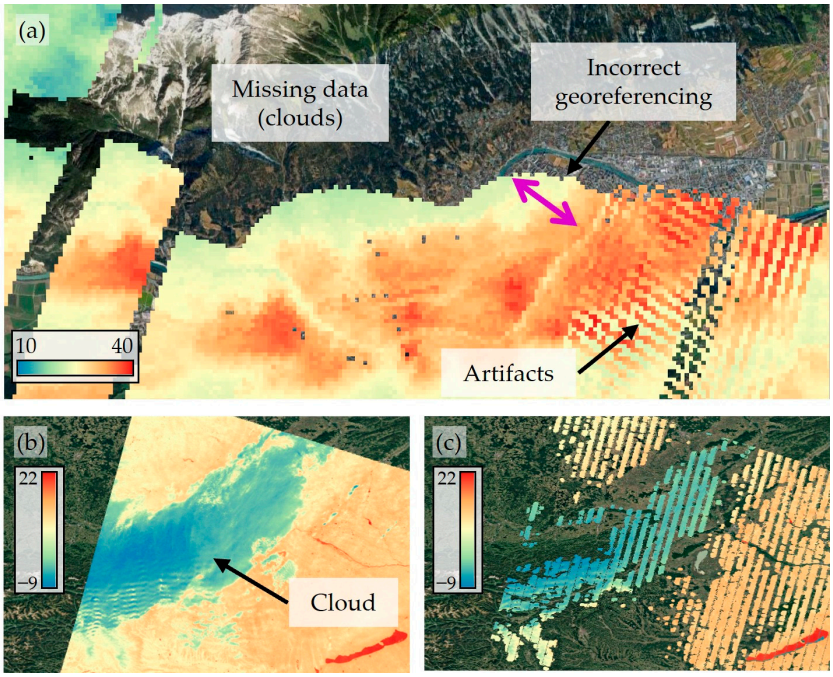

Figure 9. Examples of data quality issues for ECOSTRESS observations showing LST in °C. (**a**) Issues identified in a single observation: missing data due to masking by the ECOSTRESS-QC layer (background image visible); fringe-pattern sensor artifacts that remain even after the QC mask is applied; incorrect georeferencing (cf. position of the river in the ECOSTRESS observation and the background image, the displacement is further accentuated by the double arrow). (Location: WGS84 coordinates: 47.26646°N, 11.38075°E. Observation date and time: 11 June 2022, 14:49:19). (**b**) Summer observation before masking by the QC layer. A cloud is clearly identifiable by the negative temperature values, inconsistent with the season in which the observation was taken, as well as by the spatial extent which does not follow any spatial features in the area. (Location: WGS84 coordinates: 47.1852°N, 16.8806°E. Observation date and time: 9 July 2022, 03:02:29). (**c**) The same observation as in (**b**) after masking by the QC layer, demonstrating that the cloud was not sufficiently masked.

Furthermore, the inclusion of in situ temperature measurements to validate and complement remote sensing LST data should be considered. Planned ground truth validation activities focus on using data from the black ice monitoring system in Upper Austria, where sensors embedded in roads provide high-precision point measurements of surface temperature. Despite these data being limited to one surface type, they serve as valuable reference points for model validation. By integrating in situ data, future studies can bridge the gap between modeled predictions and real-world conditions, thus providing more robust datasets for urban heat monitoring. Additionally, model comparisons are planned using satellite-derived datasets from commercial satellite operators like OroraTech [119] and Constellr [120], although alignment between timestamps and resolutions remains a challenge.

Finally, a thorough evaluation of the INCA dataset should be conducted in future studies and larger-scale applications of our methodology, especially outside of urban regions, as it is a model-based dataset. Previous validations have demonstrated high accuracy for air temperature, while wind speed data, although generally acceptable, shows deviations, particularly in complex mountainous terrains such as peaks and valleys [74]. The accuracy of INCA data is important for achieving reliable LST estimation and overall model performance. Given that INCA is the only dataset matching the exact time of the ECOSTRESS observation, it plays an essential role in attaining the temporal gap-filling and density of LST predictions. Ensuring the reliability of input models like INCA is thus crucial for improving the predictive quality of downstream applications.

5. Conclusions

This study presents a deep-learning-based methodology for estimating land surface temperature (LST) using a combination of multi-source and multi-resolution meteorological, land cover, and satellite data, including the ECOSTRESS LST data. The proposed convolutional neural network model demonstrates promising results in generating a gap-filled LST time series over large areas at medium to high spatial resolution (<100 m). We showed that the generated LST predictions lead to at least 80% of the pixel errors falling within an acceptable ± 3 °C range. Unlike traditional satellite-based techniques, our model leverages high-resolution meteorological data to capture diurnal variations, allowing for more robust LST predictions across different regions and time periods. The proposed methodology is timely and can be applied to a variety of fields including urban planning, climate resilience, and real-time heat stress monitoring, with the goal of supporting spatial planning and climate change adaptation activities.

While the model offers robust performance over extended time periods and large areas, several challenges remain, particularly in terms of error traceability, ECOSTRESS data quality, and limitations related to model-based inputs such as INCA. Future work should focus on addressing these limitations by integrating ground truth measurements for improved validation. Through continued refinement and validation, the approach holds significant potential to support climate adaptation strategies and to improve our understanding of land use and climate interactions.

Author Contributions: Conceptualization, M.R. and K.K.; methodology, K.K. and D.C.; software, K.K. and D.C.; validation, D.C.; formal analysis, K.K. and D.C.; investigation, K.K. and D.C.; resources, K.K. and D.C.; data curation, K.K.; writing—original draft preparation, K.K., D.C. and M.R.; writing—review and editing, M.R., K.K. and M.S.; visualization, K.K. and D.C.; supervision, M.R. and M.S.; project administration, M.S.; funding acquisition, M.R. All authors have read and agreed to the published version of the manuscript.

Funding: We would like to thank the European Space Agency (ESA) for funding the project "HeatAdapt: Monitoring and mitigating heat hotspot areas", under which the presented research has been conducted.

Data Availability Statement: The data that support the findings of this study are openly available at https://gtif.esa.int (accessed on 12 January 2025).

Acknowledgments: The authors are grateful for the fruitful and illuminating discussions with Patrick Griffiths and Francesca Elisa Leonelli. The authors also want to thank the five anonymous reviewers for their constructive feedback, which helped to improve the manuscript.

Conflicts of Interest: All Authors were employed by the company GeoVille Information Systems and Data Processing GmbH. The authors declare no conflicts of interest.

References

1. Turek-Hankins, L.L.; Coughlan de Perez, E.; Scarpa, G.; Ruiz-Diaz, R.; Schwerdtle, P.N.; Joe, E.T.; Galappaththi, E.K.; French, E.M.; Austin, S.E.; Singh, C.; et al. Climate Change Adaptation to Extreme Heat: A Global Systematic Review of Implemented Action. *Oxf. Open Clim. Chan.* **2021**, *1*, kgab005. [CrossRef]
2. Oke, T.R. The Energetic Basis of the Urban Heat Island. *Q. J. R. Meteorol. Soc.* **1982**, *108*, 1–24. [CrossRef]
3. Oke, T.R.; Mills, G.; Christen, A.; Voogt, J.A. *Urban Climates*; Cambridge University Press: Cambridge, UK, 2017; ISBN 978-1-139-01647-6.
4. Deilami, K.; Kamruzzaman, M.; Liu, Y. Urban Heat Island Effect: A Systematic Review of Spatio-Temporal Factors, Data, Methods, and Mitigation Measures. *Int. J. Appl. Earth Obs. Geoinf.* **2018**, *67*, 30–42. [CrossRef]
5. Logan, T.M.; Zaitchik, B.; Guikema, S.; Nisbet, A. Night and Day: The Influence and Relative Importance of Urban Characteristics on Remotely Sensed Land Surface Temperature. *Remote Sens. Environ.* **2020**, *247*, 111861. [CrossRef]
6. Back, Y.; Bach, P.M.; Jasper-Tönnies, A.; Rauch, W.; Kleidorfer, M. A Rapid Fine-Scale Approach to Modelling Urban Bioclimatic Conditions. *Sci. Total Environ.* **2021**, *756*, 143732. [CrossRef]

7. Back, Y.; Kumar, P.; Bach, P.M.; Rauch, W.; Kleidorfer, M. Integrating CFD-GIS Modelling to Refine Urban Heat and Thermal Comfort Assessment. *Sci. Total Environ.* **2023**, *858*, 159729. [CrossRef]
8. Hart, M.A.; Sailor, D.J. Quantifying the Influence of Land-Use and Surface Characteristics on Spatial Variability in the Urban Heat Island. *Theor. Appl. Climatol.* **2009**, *95*, 397–406. [CrossRef]
9. Patel, S.; Indraganti, M.; Jawarneh, R.N. A Comprehensive Systematic Review: Impact of Land Use/ Land Cover (LULC) on Land Surface Temperatures (LST) and Outdoor Thermal Comfort. *Build. Environ.* **2024**, *249*, 111130. [CrossRef]
10. Kumar, P.; Debele, S.E.; Khalili, S.; Halios, C.H.; Sahani, J.; Aghamohammadi, N.; de Andrade, M.F.; Athanassiadou, M.; Bhui, K.; Calvillo, N.; et al. Urban Heat Mitigation by Green and Blue Infrastructure: Drivers, Effectiveness, and Future Needs. *Innovation* **2024**, *5*, 100588. [CrossRef] [PubMed]
11. Karimi, A.; Mohammad, P.; García-Martínez, A.; Moreno-Rangel, D.; Gachkar, D.; Gachkar, S. New Developments and Future Challenges in Reducing and Controlling Heat Island Effect in Urban Areas. *Environ. Dev. Sustain.* **2023**, *25*, 10485–10531. [CrossRef]
12. Greene, S.; Kalkstein, L.S.; Mills, D.M.; Samenow, J. An Examination of Climate Change on Extreme Heat Events and Climate–Mortality Relationships in Large U.S. Cities. *Weather Clim. Soc.* **2011**, *3*, 281–292. [CrossRef]
13. Vicedo-Cabrera, A.M.; Scovronick, N.; Sera, F.; Royé, D.; Schneider, R.; Tobias, A.; Astrom, C.; Guo, Y.; Honda, Y.; Hondula, D.M.; et al. The Burden of Heat-Related Mortality Attributable to Recent Human-Induced Climate Change. *Nat. Clim. Chang.* **2021**, *11*, 492–500. [CrossRef] [PubMed]
14. Covert, H.H.; Abdoel Wahid, F.; Wenzel, S.E.; Lichtveld, M.Y. Climate Change Impacts on Respiratory Health: Exposure, Vulnerability, and Risk. *Physiol. Rev.* **2023**, *103*, 2507–2522. [CrossRef] [PubMed]
15. Terzi, S.; Torresan, S.; Schneiderbauer, S.; Critto, A.; Zebisch, M.; Marcomini, A. Multi-Risk Assessment in Mountain Regions: A Review of Modelling Approaches for Climate Change Adaptation. *J. Environ. Manag.* **2019**, *232*, 759–771. [CrossRef] [PubMed]
16. Intergovernmental Panel on Climate Change (IPCC). *Climate Change 2022—Impacts, Adaptation and Vulnerability: Working Group II Contribution to the Sixth Assessment Report of the Intergovernmental Panel on Climate Change*; Cambridge University Press: Cambridge, UK, 2023; ISBN 978-1-00-932584-4.
17. Cheval, S.; Amihăesei, V.-A.; Chitu, Z.; Dumitrescu, A.; Falcescu, V.; Irașoc, A.; Micu, D.M.; Mihulet, E.; Ontel, I.; Paraschiv, M.-G.; et al. A Systematic Review of Urban Heat Island and Heat Waves Research (1991–2022). *Clim. Risk Manag.* **2024**, *44*, 100603. [CrossRef]
18. Li, H.; Zhou, Y.; Li, X.; Meng, L.; Wang, X.; Wu, S.; Sodoudi, S. A New Method to Quantify Surface Urban Heat Island Intensity. *Sci. Total Environ.* **2018**, *624*, 262–272. [CrossRef]
19. Yang, Q.; Huang, X.; Yang, J.; Liu, Y. The Relationship between Land Surface Temperature and Artificial Impervious Surface Fraction in 682 Global Cities: Spatiotemporal Variations and Drivers. *Environ. Res. Lett.* **2021**, *16*, 024032. [CrossRef]
20. Bowen, I.S. The Ratio of Heat Losses by Conduction and by Evaporation from Any Water Surface. *Phys. Rev.* **1926**, *27*, 779–787. [CrossRef]
21. Mahmood, R.; Pielke, R.A., Sr.; Hubbard, K.G.; Niyogi, D.; Dirmeyer, P.A.; McAlpine, C.; Carleton, A.M.; Hale, R.; Gameda, S.; Beltrán-Przekurat, A.; et al. Land Cover Changes and Their Biogeophysical Effects on Climate. *Int. J. Climatol.* **2014**, *34*, 929–953. [CrossRef]
22. Schwingshackl, C.; Hirschi, M.; Seneviratne, S.I. Quantifying Spatiotemporal Variations of Soil Moisture Control on Surface Energy Balance and Near-Surface Air Temperature. *J. Clim.* **2017**, *30*, 7105–7124. [CrossRef]
23. Li, D.; Liao, W.; Rigden, A.J.; Liu, X.; Wang, D.; Malyshev, S.; Shevliakova, E. Urban Heat Island: Aerodynamics or Imperviousness? *Sci. Adv.* **2019**, *5*, eaau4299. [CrossRef]
24. Anderson, M.C.; Norman, J.M.; Kustas, W.P.; Houborg, R.; Starks, P.J.; Agam, N. A Thermal-Based Remote Sensing Technique for Routine Mapping of Land-Surface Carbon, Water and Energy Fluxes from Field to Regional Scales. *Remote Sens. Environ.* **2008**, *112*, 4227–4241. [CrossRef]
25. Dash, P.; Göttsche, F.-M.; Olesen, F.-S.; Fischer, H. Land Surface Temperature and Emissivity Estimation from Passive Sensor Data: Theory and Practice-Current Trends. *Int. J. Remote Sens.* **2002**, *23*, 2563–2594. [CrossRef]
26. Dickinson, R.E. Land Surface Processes and Climate—Surface Albedos and Energy Balance. In *Theory of Climate*; Elsevier: Berlin/Heidelberg, Germany, 1983.
27. Zhou, D.; Xiao, J.; Bonafoni, S.; Berger, C.; Deilami, K.; Zhou, Y.; Frolking, S.; Yao, R.; Qiao, Z.; Sobrino, J.A. Satellite Remote Sensing of Surface Urban Heat Islands: Progress, Challenges, and Perspectives. *Remote Sens.* **2019**, *11*, 48. [CrossRef]
28. Wesley, E.J.; Brunsell, N.A. Greenspace Pattern and the Surface Urban Heat Island: A Biophysically-Based Approach to Investigating the Effects of Urban Landscape Configuration. *Remote Sens.* **2019**, *11*, 2322. [CrossRef]
29. Granero-Belinchon, C.; Michel, A.; Lagouarde, J.-P.; Sobrino, J.A.; Briottet, X. Night Thermal Unmixing for the Study of Microscale Surface Urban Heat Islands with TRISHNA-Like Data. *Remote Sens.* **2019**, *11*, 1449. [CrossRef]
30. Cammalleri, C.; Vogt, J. On the Role of Land Surface Temperature as Proxy of Soil Moisture Status for Drought Monitoring in Europe. *Remote Sens.* **2015**, *7*, 16849–16864. [CrossRef]

31. Sun, J.; Salvucci, G.D.; Entekhabi, D. Estimates of Evapotranspiration from MODIS and AMSR-E Land Surface Temperature and Moisture over the Southern Great Plains. *Remote Sens. Environ.* **2012**, *127*, 44–59. [CrossRef]
32. Galleguillos, M.; Jacob, F.; Prévot, L.; French, A.; Lagacherie, P. Comparison of Two Temperature Differencing Methods to Estimate Daily Evapotranspiration over a Mediterranean Vineyard Watershed from ASTER Data. *Remote Sens. Environ.* **2011**, *115*, 1326–1340. [CrossRef]
33. Belward, A.; Bourassa, M.A.; Dowell, M.; Briggs, S. *The Global Observing System for Climate: Implementation Needs*; Global Climate Observing System: Geneva, Switzerland, 2016.
34. Yu, Y.; Liu, Y.; Yu, P. Land Surface Temperature Product Development for JPSS and GOES-R Missions. In *Comprehensive Remote Sensing*; Elsevier: Berlin/Heidelberg, Germany, 2018.
35. Becker, F.; Li, Z. Surface Temperature and Emissivity at Various Scales: Definition, Measurement and Related Problems. *Remote Sens. Rev.* **1995**, *12*, 225–253. [CrossRef]
36. Dash, P.; Göttsche, F.-M.; Olesen, F.-S.; Fischer, H. Retrieval of Land Surface Temperature and Emissivity from Satellite Data: Physics, Theoretical Limitations and Current Methods. *J. Indian Soc. Remote Sens.* **2001**, *29*, 23–30. [CrossRef]
37. Qin, Z.; Karnieli, A. Progress in the Remote Sensing of Land Surface Temperature and Ground Emissivity Using NOAA-AVHRR Data. *Int. J. Remote Sens.* **1999**, *20*, 2367–2393. [CrossRef]
38. Li, Z.-L.; Wu, H.; Duan, S.-B.; Zhao, W.; Ren, H.; Liu, X.; Leng, P.; Tang, R.; Ye, X.; Zhu, J.; et al. Satellite Remote Sensing of Global Land Surface Temperature: Definition, Methods, Products, and Applications. *Rev. Geophys.* **2023**, *61*, e2022RG000777. [CrossRef]
39. Prata, A.J.; Caselles, V.; Coll, C.; Sobrino, J.A.; Ottlé, C. Thermal Remote Sensing of Land Surface Temperature from Satellites: Current Status and Future Prospects. *Remote Sens. Rev.* **1995**, *12*, 175–224. [CrossRef]
40. Wark, D.Q.; Yamamoto, G.; Lienesch, J.H. Methods of Estimating Infrared Flux and Surface Temperature from Meteorological Satellites. *J. Atmos. Sci.* **1962**, *19*, 369–384. [CrossRef]
41. Lee, J.; Dessler, A.E. Improved Surface Urban Heat Impact Assessment Using GOES Satellite Data: A Comparative Study with ERA-5. *Geophys. Res. Lett.* **2024**, *51*, e2023GL107364. [CrossRef]
42. Gouveia, C.M.; Martins, J.P.A.; Russo, A.; Durão, R.; Trigo, I.F. Monitoring Heat Extremes across Central Europe Using Land Surface Temperature Data Records from SEVIRI/MSG. *Remote Sens.* **2022**, *14*, 3470. [CrossRef]
43. Reiners, P.; Holzwarth, S.; Dietz, A.; Bachmann, M.; Sobrino, J.; Kuenzer, C. Fusing AVHRR LST with Geostationary SEVIRI LST to Create a Long-Term Daily Maximum LST Time Series over Europe. *IEEE J. Sel. Top. Appl. Earth Obs. Remote Sens.* **2024**, *18*, 2168–2189. [CrossRef]
44. Yu, P.; Zhao, T.; Shi, J.; Ran, Y.; Jia, L.; Ji, D.; Xue, H. Global Spatiotemporally Continuous MODIS Land Surface Temperature Dataset. *Sci. Data* **2022**, *9*, 143. [CrossRef]
45. Prata, A.J. *Land Surface Temperature Measurement from Space: AATSR Algorithm Theoretical Basis Document*; Contract Report to ESA, CSIRO Atmospheric Research; CSIRO: Aspendale, VIC, Australia, 2002; pp. 1–34.
46. Hulley, G.C.; Malakar, N.K.; Islam, T.; Freepartner, R.J. NASA's MODIS and VIIRS Land Surface Temperature and Emissivity Products: A Long-Term and Consistent Earth System Data Record. *IEEE J. Sel. Top. Appl. Earth Obs. Remote Sens.* **2018**, *11*, 522–535. [CrossRef]
47. Sentinel-1 Team. *Sentinel-1 User Handbook*; ESA Communications: Noordwijk, The Netherlands, 2013; p. 774.
48. Hulley, G.C.; Hook, S.J. Generating Consistent Land Surface Temperature and Emissivity Products Between ASTER and MODIS Data for Earth Science Research. *IEEE Trans. Geosci. Remote Sens.* **2011**, *49*, 1304–1315. [CrossRef]
49. Malakar, N.K.; Hulley, G.C.; Hook, S.J.; Laraby, K.; Cook, M.; Schott, J.R. An Operational Land Surface Temperature Product for Landsat Thermal Data: Methodology and Validation. *IEEE Trans. Geosci. Remote Sens.* **2018**, *56*, 5717–5735. [CrossRef]
50. Hulley, G.C.; Gottsche, F.M.; Rivera, G.; Hook, S.J.; Freepartner, R.J.; Martin, M.A.; Cawse-Nicholson, K.; Johnson, W.R. Validation and Quality Assessment of the ECOSTRESS Level-2 Land Surface Temperature and Emissivity Product. *IEEE Trans. Geosci. Remote Sens.* **2022**, *60*, 1–23. [CrossRef]
51. De Almeida, C.R.; Teodoro, A.C.; Gonçalves, A. Study of the Urban Heat Island (UHI) Using Remote Sensing Data/Techniques: A Systematic Review. *Environments* **2021**, *8*, 105. [CrossRef]
52. Manoli, G.; Fatichi, S.; Bou-Zeid, E.; Katul, G.G. Seasonal Hysteresis of Surface Urban Heat Islands. *Proc. Natl. Acad. Sci. USA* **2020**, *117*, 7082–7089. [CrossRef] [PubMed]
53. Dian, C.; Pongrácz, R.; Dezső, Z.; Bartholy, J. Annual and Monthly Analysis of Surface Urban Heat Island Intensity with Respect to the Local Climate Zones in Budapest. *Urban Clim.* **2020**, *31*, 100573. [CrossRef]
54. Benz, S.A.; Burney, J.A. Widespread Race and Class Disparities in Surface Urban Heat Extremes Across the United States. *Earths Future* **2021**, *9*, e2021EF002016. [CrossRef]
55. Peng, S.; Piao, S.; Ciais, P.; Friedlingstein, P.; Ottle, C.; Bréon, F.-M.; Nan, H.; Zhou, L.; Myneni, R.B. Surface Urban Heat Island Across 419 Global Big Cities. *Environ. Sci. Technol.* **2012**, *46*, 696–703. [CrossRef] [PubMed]

56. Sobrino, J.A.; Oltra-Carrió, R.; Sòria, G.; Jiménez-Muñoz, J.C.; Franch, B.; Hidalgo, V.; Mattar, C.; Julien, Y.; Cuenca, J.; Romaguera, M.; et al. Evaluation of the Surface Urban Heat Island Effect in the City of Madrid by Thermal Remote Sensing. *Int. J. Remote Sens.* **2013**, *34*, 3177–3192. [CrossRef]
57. Zhou, J.; Liu, S.; Li, M.; Zhan, W.; Xu, Z.; Xu, T. Quantification of the Scale Effect in Downscaling Remotely Sensed Land Surface Temperature. *Remote Sens.* **2016**, *8*, 975. [CrossRef]
58. Zhou, B.; Rybski, D.; Kropp, J.P. The Role of City Size and Urban Form in the Surface Urban Heat Island. *Sci. Rep.* **2017**, *7*, 4791. [CrossRef]
59. Onačillová, K.; Gallay, M.; Paluba, D.; Péliová, A.; Tokarčík, O.; Laubertová, D. Combining Landsat 8 and Sentinel-2 Data in Google Earth Engine to Derive Higher Resolution Land Surface Temperature Maps in Urban Environment. *Remote Sens.* **2022**, *14*, 4076. [CrossRef]
60. Pu, R. Assessing Scaling Effect in Downscaling Land Surface Temperature in a Heterogenous Urban Environment. *Int. J. Appl. Earth Obs. Geoinf.* **2021**, *96*, 102256. [CrossRef]
61. Pu, R.; Bonafoni, S. Reducing Scaling Effect on Downscaled Land Surface Temperature Maps in Heterogenous Urban Environments. *Remote Sens.* **2021**, *13*, 5044. [CrossRef]
62. Pu, R.; Bonafoni, S. Thermal Infrared Remote Sensing Data Downscaling Investigations: An Overview on Current Status and Perspectives. *Remote Sens. Appl. Soc. Environ.* **2023**, *29*, 100921. [CrossRef]
63. Masson, V.; Heldens, W.; Bocher, E.; Bonhomme, M.; Bucher, B.; Burmeister, C.; de Munck, C.; Esch, T.; Hidalgo, J.; Kanani-Sühring, F.; et al. City-Descriptive Input Data for Urban Climate Models: Model Requirements, Data Sources and Challenges. *Urban Clim.* **2020**, *31*, 100536. [CrossRef]
64. Shen, H.; Li, X.; Cheng, Q.; Zeng, C.; Yang, G.; Li, H.; Zhang, L. Missing Information Reconstruction of Remote Sensing Data: A Technical Review. *IEEE Geosci. Remote Sens.* **2015**, *3*, 61–85. [CrossRef]
65. Wu, P.; Yin, Z.; Zeng, C.; Duan, S.-B.; Göttsche, F.-M.; Ma, X.; Li, X.; Yang, H.; Shen, H. Spatially Continuous and High-Resolution Land Surface Temperature Product Generation: A Review of Reconstruction and Spatiotemporal Fusion Techniques. *IEEE Geosci. Remote Sens.* **2021**, *9*, 112–137. [CrossRef]
66. Mo, Y.; Xu, Y.; Chen, H.; Zhu, S. A Review of Reconstructing Remotely Sensed Land Surface Temperature Under Cloudy Conditions. *Remote Sens.* **2021**, *13*, 2838. [CrossRef]
67. Jia, A.; Liang, S.; Wang, D.; Mallick, K.; Zhou, S.; Hu, T.; Xu, S. Advances in Methodology and Generation of All-Weather Land Surface Temperature Products From Polar-Orbiting and Geostationary Satellites: A Comprehensive Review. *IEEE Geosci. Remote Sens.* **2024**, *12*, 218–260. [CrossRef]
68. Wu, P.; Yin, Z.; Yang, H.; Wu, Y.; Ma, X. Reconstructing Geostationary Satellite Land Surface Temperature Imagery Based on a Multiscale Feature Connected Convolutional Neural Network. *Remote Sens.* **2019**, *11*, 300. [CrossRef]
69. Ke, L.; Ding, X.; Song, C. Reconstruction of Time-Series MODIS LST in Central Qinghai-Tibet Plateau Using Geostatistical Approach. *IEEE Geosci. Remote Sens.* **2013**, *10*, 1602–1606. [CrossRef]
70. Zhang, G.; Xiao, X.; Dong, J.; Kou, W.; Jin, C.; Qin, Y.; Zhou, Y.; Wang, J.; Menarguez, M.A.; Biradar, C. Mapping Paddy Rice Planting Areas through Time Series Analysis of MODIS Land Surface Temperature and Vegetation Index Data. *ISPRS J. Photogramm. Remote Sens.* **2015**, *106*, 157–171. [CrossRef]
71. Weiss, D.J.; Atkinson, P.M.; Bhatt, S.; Mappin, B.; Hay, S.I.; Gething, P.W. An Effective Approach for Gap-Filling Continental Scale Remotely Sensed Time-Series. *ISPRS J. Photogramm. Remote Sens.* **2014**, *98*, 106–118. [CrossRef]
72. Sarafanov, M.; Kazakov, E.; Nikitin, N.O.; Kalyuzhnaya, A.V. A Machine Learning Approach for Remote Sensing Data Gap-Filling with Open-Source Implementation: An Example Regarding Land Surface Temperature, Surface Albedo and NDVI. *Remote Sens.* **2020**, *12*, 3865. [CrossRef]
73. Duan, S.-B.; Li, Z.-L.; Leng, P. A Framework for the Retrieval of All-Weather Land Surface Temperature at a High Spatial Resolution from Polar-Orbiting Thermal Infrared and Passive Microwave Data. *Remote Sens. Environ.* **2017**, *195*, 107–117. [CrossRef]
74. Zeng, C.; Long, D.; Shen, H.; Wu, P.; Cui, Y.; Hong, Y. A Two-Step Framework for Reconstructing Remotely Sensed Land Surface Temperatures Contaminated by Cloud. *ISPRS J. Photogramm. Remote Sens.* **2018**, *141*, 30–45. [CrossRef]
75. Jia, A.; Ma, H.; Liang, S.; Wang, D. Cloudy-Sky Land Surface Temperature from VIIRS and MODIS Satellite Data Using a Surface Energy Balance-Based Method. *Remote Sens. Environ.* **2021**, *263*, 112566. [CrossRef]
76. Liu, Z.; Wu, P.; Duan, S.; Zhan, W.; Ma, X.; Wu, Y. Spatiotemporal Reconstruction of Land Surface Temperature Derived From FengYun Geostationary Satellite Data. *IEEE J. Sel. Top. Appl. Earth Obs. Remote Sens.* **2017**, *10*, 4531–4543. [CrossRef]
77. Ma, J.; Shen, H.; Wu, P.; Wu, J.; Gao, M.; Meng, C. Generating Gapless Land Surface Temperature with a High Spatio-Temporal Resolution by Fusing Multi-Source Satellite-Observed and Model-Simulated Data. *Remote Sens. Environ.* **2022**, *278*, 113083. [CrossRef]
78. Belgiu, M.; Stein, A. Spatiotemporal Image Fusion in Remote Sensing. *Remote Sens.* **2019**, *11*, 818. [CrossRef]

79. Zhu, X.X.; Tuia, D.; Mou, L.; Xia, G.-S.; Zhang, L.; Xu, F.; Fraundorfer, F. Deep Learning in Remote Sensing: A Comprehensive Review and List of Resources. *IEEE Geosci. Remote Sens.* **2017**, *5*, 8–36. [CrossRef]
80. Ball, J.E.; Anderson, D.T.; Chan, C.S., Sr. Comprehensive Survey of Deep Learning in Remote Sensing: Theories, Tools, and Challenges for the Community. *J. Appl. Remote Sens.* **2017**, *11*, 042609. [CrossRef]
81. Chlingaryan, A.; Sukkarieh, S.; Whelan, B. Machine Learning Approaches for Crop Yield Prediction and Nitrogen Status Estimation in Precision Agriculture: A Review. *Comput. Electron. Agric.* **2018**, *151*, 61–69. [CrossRef]
82. Osco, L.P.; Marcato Junior, J.; Marques Ramos, A.P.; de Castro Jorge, L.A.; Fatholahi, S.N.; de Andrade Silva, J.; Matsubara, E.T.; Pistori, H.; Gonçalves, W.N.; Li, J. A Review on Deep Learning in UAV Remote Sensing. *Int. J. Appl. Earth Obs. Geoinf.* **2021**, *102*, 102456. [CrossRef]
83. Li, J.; Hong, D.; Gao, L.; Yao, J.; Zheng, K.; Zhang, B.; Chanussot, J. Deep Learning in Multimodal Remote Sensing Data Fusion: A Comprehensive Review. *Int. J. Appl. Earth Obs. Geoinf.* **2022**, *112*, 102926. [CrossRef]
84. Yuan, Q.; Shen, H.; Li, T.; Li, Z.; Li, S.; Jiang, Y.; Xu, H.; Tan, W.; Yang, Q.; Wang, J.; et al. Deep Learning in Environmental Remote Sensing: Achievements and Challenges. *Remote Sens. Environ.* **2020**, *241*, 111716. [CrossRef]
85. Wang, Q.; Tang, Y.; Tong, X.; Atkinson, P.M. Filling Gaps in Cloudy Landsat LST Product by Spatial-Temporal Fusion of Multi-Scale Data. *Remote Sens. Environ.* **2024**, *306*, 114142. [CrossRef]
86. Wu, P.; Su, Y.; Duan, S.; Li, X.; Yang, H.; Zeng, C.; Ma, X.; Wu, Y.; Shen, H. A Two-Step Deep Learning Framework for Mapping Gapless All-Weather Land Surface Temperature Using Thermal Infrared and Passive Microwave Data. *Remote Sens. Environ.* **2022**, *277*, 113070. [CrossRef]
87. Kartal, S.; Sekertekin, A. Prediction of MODIS Land Surface Temperature Using New Hybrid Models Based on Spatial Interpolation Techniques and Deep Learning Models. *Environ. Sci. Pollut. Res.* **2022**, *29*, 67115–67134. [CrossRef]
88. Tan, J.; NourEldeen, N.; Mao, K.; Shi, J.; Li, Z.; Xu, T.; Yuan, Z. Deep Learning Convolutional Neural Network for the Retrieval of Land Surface Temperature from AMSR2 Data in China. *Sensors* **2019**, *19*, 2987. [CrossRef] [PubMed]
89. Zhang, H.; Tang, B.-H.; Li, Z.-L. A Practical Two-Step Framework for All-Sky Land Surface Temperature Estimation. *Remote Sens. Environ.* **2024**, *303*, 113991. [CrossRef]
90. Huang, B.; Zhao, B.; Song, Y. Urban Land-Use Mapping Using a Deep Convolutional Neural Network with High Spatial Resolution Multispectral Remote Sensing Imagery. *Remote Sens. Environ.* **2018**, *214*, 73–86. [CrossRef]
91. Cheng, G.; Xie, X.; Han, J.; Guo, L.; Xia, G.-S. Remote Sensing Image Scene Classification Meets Deep Learning: Challenges, Methods, Benchmarks, and Opportunities. *IEEE J. Sel. Top. Appl. Earth Obs. Remote Sens.* **2020**, *13*, 3735–3756. [CrossRef]
92. Corbane, C.; Syrris, V.; Sabo, F.; Politis, P.; Melchiorri, M.; Pesaresi, M.; Soille, P.; Kemper, T. Convolutional Neural Networks for Global Human Settlements Mapping from Sentinel-2 Satellite Imagery. *Neural Comput. Appl.* **2021**, *33*, 6697–6720. [CrossRef]
93. Mansourmoghaddam, M.; Rousta, I.; Ghafarian Malamiri, H.; Sadeghnejad, M.; Krzyszczak, J.; Ferreira, C.S.S. Modeling and Estimating the Land Surface Temperature (LST) Using Remote Sensing and Machine Learning (Case Study: Yazd, Iran). *Remote Sens.* **2024**, *16*, 454. [CrossRef]
94. Han, J.; Fang, S.; Mi, Q.; Wang, X.; Yu, Y.; Zhuo, W.; Peng, X. A Time-Continuous Land Surface Temperature (LST) Data Fusion Approach Based on Deep Learning with Microwave Remote Sensing and High-Density Ground Truth Observations. *Sci. Total Environ.* **2024**, *914*, 169992. [CrossRef] [PubMed]
95. Climate Data for Innsbruck. Available online: https://en.wikipedia.org/wiki/Innsbruck (accessed on 7 June 2024).
96. Climate Data for Vienna. Available online: https://en.wikipedia.org/wiki/vienna (accessed on 7 June 2024).
97. Oke, T.R. *Boundary Layer Climates*, 2nd ed.; Routledge: London, UK, 1987.
98. Matzarakis, A.; Rutz, F.; Mayer, H. Modelling Radiation Fluxes in Simple and Complex Environments: Basics of the RayMan Model. *Int. J. Biometeorol.* **2010**, *54*, 131–139. [CrossRef] [PubMed]
99. Li, Z.-L.; Tang, B.-H.; Wu, H.; Ren, H.; Yan, G.; Wan, Z.; Trigo, I.F.; Sobrino, J.A. Satellite-Derived Land Surface Temperature: Current Status and Perspectives. *Remote Sens. Environ.* **2013**, *131*, 14–37. [CrossRef]
100. Xuanlan, Z.; Junbang, W.; Hui, Y.; Amir, M.; Shaoqiang, W. The Bowen Ratio of an Alpine Grassland in Three-River Headwaters, Qinghai-Tibet Plateau, from 2001 to 2018. *J. Resour. Ecol.* **2021**, *12*, 305–318. [CrossRef]
101. Hulley, G.; Freepartner, R. *ECOsystem Spaceborne Thermal Radiometer Experiment on Space Station (ECOSTRESS): Mission Level 2 Product User Guide*; California Institute of Technology: Pasadena, CA, USA; Jet Propulsion Laboratory: Flintridge, CA, USA, 2019.
102. Goffin, B.D.; Cortés-Monroy, C.C.; Neira-Román, F.; Gupta, D.D.; Lakshmi, V. At Which Overpass Time Do ECOSTRESS Observations Best Align with Crop Health and Water Rights? *Remote Sens.* **2024**, *16*, 3174. [CrossRef]
103. NASA Earthdata Search Application. Available online: https://search.earthdata.nasa.gov (accessed on 13 June 2024).
104. Haiden, T.; Kann, A.; Wittmann, C.; Pistotnik, G.; Bica, B.; Gruber, C. The Integrated Nowcasting through Comprehensive Analysis (INCA) System and Its Validation over the Eastern Alpine Region. *Weather Forecast.* **2011**, *26*, 166–183. [CrossRef]
105. Ghaemi, E.; Foelsche, U.; Kann, A.; Fuchsberger, J. Evaluation of Integrated Nowcasting through Comprehensive Analysis (INCA) Precipitation Analysis Using a Dense Rain-Gauge Network in Southeastern Austria. *Hydrol. Earth Syst. Sci.* **2021**, *25*, 4335–4356. [CrossRef]

106. GeoSphere Austria Data Hub. Available online: https://data.hub.geosphere.at (accessed on 13 June 2024).
107. Google Cloud Sentinel-2 Data Collection. Available online: https://cloud.google.com/storage/docs/public-datasets/sentinel-2 (accessed on 13 June 2024).
108. EEA Datahub. Available online: https://sdi.eea.europa.eu/catalogue/datahub (accessed on 13 June 2024).
109. Copernicus Land Monitoring Service. Available online: https://land.copernicus.eu (accessed on 13 June 2024).
110. ECOSTRESS Swath to Grid Conversion Repository. Available online: https://git.earthdata.nasa.gov/projects/LPDUR/repos/ecostress_swath2grid (accessed on 13 June 2024).
111. Syrris, V.; Hasenohr, P.; Delipetrev, B.; Kotsev, A.; Kempeneers, P.; Soille, P. Evaluation of the Potential of Convolutional Neural Networks and Random Forests for Multi-Class Segmentation of Sentinel-2 Imagery. *Remote Sens.* **2019**, *11*, 907. [CrossRef]
112. Ioffe, S.; Szegedy, C. Batch Normalization: Accelerating Deep Network Training by Reducing Internal Covariate Shift. *arXiv* **2015**, arXiv:1502.03167.
113. Srivastava, N.; Hinton, G.; Krizhevsky, A.; Sutskever, I.; Salakhutdinov, R. Dropout: A Simple Way to Prevent Neural Networks from Overfitting. *J. Mach. Learn. Res.* **2014**, *15*, 1929–1958.
114. Yang, Y.; Zhao, W.; Yang, Y.; Xu, M.; Mukhtar, H.; Tauqir, G.; Tarolli, P. An Annual Temperature Cycle Feature Constrained Method for Generating MODIS Daytime All-Weather Land Surface Temperature. *IEEE Trans. Geosci. Remote Sens.* **2024**, *62*, 4405014. [CrossRef]
115. Naserikia, M.; Hart, M.A.; Nazarian, N.; Bechtel, B.; Lipson, M.; Nice, K.A. Land Surface and Air Temperature Dynamics: The Role of Urban Form and Seasonality. *Sci. Total Environ.* **2023**, *905*, 167306. [CrossRef]
116. Tang, B.-H.; Zhan, C.; Li, Z.-L.; Wu, H.; Tang, R. Estimation of Land Surface Temperature From MODIS Data for the Atmosphere with Air Temperature Inversion Profile. *IEEE J. Sel. Top. Appl. Earth Obs. Remote Sens.* **2017**, *10*, 2976–2983. [CrossRef]
117. Shi, J.; Hu, C. Evaluation of ECOSTRESS Thermal Data over South Florida Estuaries. *Sensors* **2021**, *21*, 4341. [CrossRef]
118. Gorokhovich, Y.; Cawse-Nicholson, K.; Papadopoulos, N.; Oikonomou, D. Use of ECOSTRESS Data for Measurements of the Surface Water Temperature: Significance of Data Filtering in Accuracy Assessment. *Remote Sens. Appl. Soc. Environ.* **2022**, *26*, 100739. [CrossRef]
119. OroraTech GmbH. Available online: https://ororatech.com (accessed on 1 October 2024).
120. Constellr GmbH. Available online: www.constellr.com (accessed on 1 October 2024).